Department of Physics
Kyoto University

The thermal evolution of primordial gas clouds: A clue to galaxy formation

Hajime Susa
Department of Physics, Kyoto University
Kyoto 606-01, Japan

Contents

1 Introduction **5**

2 Cooling processes in primordial gas cloud **11**
2.1 Radiative recombination 11
2.2 Collisional Ionization 12
2.3 Bound-bound transition of hydrogen atom 13
2.4 Thermal bremsstrahlung emission 16
2.5 H_2 radiative cooling (optically thin limit) 17
2.6 H_2 dissociation 19
2.7 H_2 formation 19

3 The one zone collapse model : non-spherical collapse of the primordial gas clouds **21**
3.1 Density evolution of the cloud 21
3.2 Thermal evolution and chemical reactions 22
3.3 Initial conditions 22
3.4 The limit of the calculation 23
3.5 Thermal history of the collapse 23
3.5.1 The collapse of the non-rotating clouds : $\alpha_0 \neq 1, \xi = 0$ 23
3.5.2 The collapse of rotating clouds 24
3.6 The mass of the fragments 28
3.7 Conclusions & discussion 30

4 Fragmentation of cylinder **33**
4.1 Basic equations 33
4.1.1 Equation of motion of the cloud for cylindrical collapse 33
4.1.2 Energy equation and chemical reactions 34
4.2 The epoch of fragmentation and the mass of a fragment 34
4.3 The results of numerical calculations 35
4.4 Analytical estimate of the minimum fragment mass 35
4.5 Discussions 36

5 Thermal evolution behind the shock in primordial gas : A semi-analytic approach **39**
5.1 The time scales 39
5.1.1 Ionization and cooling 41
5.1.2 Recombination and cooling 41
5.1.3 The fraction of H_2 41
5.2 Comparison with the numerical calculation 43
5.3 Conclusion 44

6 1- dimensional hydrodynamical approach **45**
6.1 Basic equations 45
6.2 Numerical method 46
6.3 Initial conditions 48
6.4 What is expected ? 48
6.5 Results and discussion 49
6.5.1 The oscillation around $T_2 = 10^4$K 49
6.5.2 The time scales 54
6.5.3 The model difference 61

7 Summary **63**

A H_2 line cooling (the expression for general value of τ for the one zone model) **66**

B Radiative Transfer **66**

C The chemical reactions **68**

D Steady shock **68**
D.1 Basic equations 70
D.2 Isobaricity of the postshock layer 70

Abstract

The thermal evolution of the primordial gas cloud is investigated. First, we study non-spherical primordial gas clouds of mass $M = 10^6 M_\odot$. We study two cases: 1) prolate and oblate clouds without angular momentum, 2) initially spherical, oblate and prolate clouds with angular momentum. In the spherical case, the magnitude of the angular momentum is the key quantity which determines the fragment mass. The fragment mass is found to be $M \gtrsim 90 M_\odot$ for $10^{-2} \lesssim \lambda \lesssim 1$, where λ is the cosmological spin parameter. For the oblate shape of initial gas clouds, the angular momentum is almost always not important. In the case of prolate clouds with some angular momentum, collapse proceeds in the same way as the spherical case, and a bounce occurs to form a disk due to the angular momentum. In any case, the estimated "fragment mass" must be almost above $90 M_\odot$ for primordial gas clouds with typical angular momentum and typical oblateness or prolateness.

Secondly, we investigate the collapse and the fragmentation of infinitely long cylinders which are assumed to emerge after the disk collapse of the initial density perturbation in the early universe. Comparing the timescale of collapse with that of fragmentation, we obtain the typical mass of a fragment both numerically and analytically. We show that the estimated mass gives the minimum mass of a fragment which is formed from the primordial gas cloud and is essentially determined by the *Chandrasekhar mass*.

Thirdly, we investigate the thermal evolution of the postshock layer of primordial gas in a steady flow approximation. Comparing the time scales of recombination, ionization, and radiative cooling processes, we find that the thermal evolution behind the shock front can easily undertood with ionization degree v.s. temperature plane.

Finally, we perform hydrodynamical calculations which represent the dynamical collapse of cool clouds formed out of density perturbation after the decoupling of universe. Very complicated spatial structures are formed and oscllation of the shock front is found. Comparing the time scale of collapse with that of fragmentation again, we also find that the fragmentation of the disk sets in at the inner region. The cooled region fragments into many cylinders, whose line densities are determined by the temperature of the cooled region. Using the argument of cylinderical collapse, we find the final fragment mass is in the range $1 M_\odot \lesssim M \lesssim 10^3 M_\odot$.

1 Introduction

How are the various structures in the universe formed ? This is one of the most basic question in astrophysics. In our universe, there are so many kinds of structures such as Large Scale Structures (LSS), the clusters of galaxies, galaxies, globular clusters, stars and so on. Almost all of those structures seem to grow out of the small departures from the homogeneity present in the early universe before the recombination epoch of the universe. In the cosmological point of view, LSS and the clusters of galaxies are very important because their sizes are so large that their formation histories directly reflect the information on the cosmological model parameters since gravitation is the only physics which is responsible for their formation. The star formation process in interstellar medium is still uncertain. Nevertheless it definitely contains many important physical processes such as nuclear reactions and radiative cooling.

The formation of galaxies, which is the subject of this thesis, is the least known process among various processes of structure formation. There are several reasons for this fact. First of all, it is difficult to observe the galaxies at the phase of their formation, because they are so far from the earth. This situation, however, is currently improved significantly by the Hubble Space Telescope (HST) and ground based huge telescopes such as Keck. The recent observations of distant galaxies tell us that the galaxies at the redshift is greater than unity have more clumpy structures than those in the neighborhood of our Galaxies (Driver et.al. 1995 [11]). The number count of the galaxies in the deep field reveals the problem "the excess of faint blue galaxies", which implies the existence of young galaxies in which the stars are forming at high redshift (Glatzebrook et.al.(1995) [15]). Secondly, from the theoretical point of view, the mass scale of galaxies ($10^8 M_\odot \lesssim M \lesssim 10^{13} M_\odot$) is the intermediate scale which is affected by both the cosmological model and many thermal processes. In other words, due to the radiative cooling, the galaxies cannot be understood just as the gravitationally collapsed density perturbations. This is the difference between the formation process of the LSS or the clusters of galaxies, and the formation of the galaxies. Finally, since *the galaxies are the clusters of stars* and what we observe is the light of the stars, we must regard the galaxy formation as the formation of stars in the primordial gas cloud. As a result, any calculation to investigate the formation of the galaxies and their stars need a very wide dynamic range. In spite of these difficulties, the theoretical investigations of the formation of galaxies from *first principles* has been proceeded since '60s.

Silk (1977) [51] and Rees & Ostriker (1977) [47] have pointed out that the mass of the galaxies are determined by a simple argument with the *cooling diagram* (Fig.1). They assume that an uniformly collapsing density perturbation which is separated from the Hubble expansion is heated up to the virial temperature by shock heating. This assumption seems to be quite reasonable, because at the galactic scales ($(10^8 M_\odot \lesssim M \lesssim 10^{13} M_\odot$) cosmological density perturbations collapse at low redshift ($1 \lesssim z \lesssim 10$) for the CDM model, and the Jeans scale of the universe at this epoch is quite smaller than $10^8 M_\odot$ unless the universe is reionized [1].

[1] If the universe is reionized, the heating due to the ionizing UV photons raise the IGM temperature, and the Jeans mass become large. However, the UV photons must come out of already formed structures, which I am going to investigate in this thesis. As a result, the formation of first object is not affected by

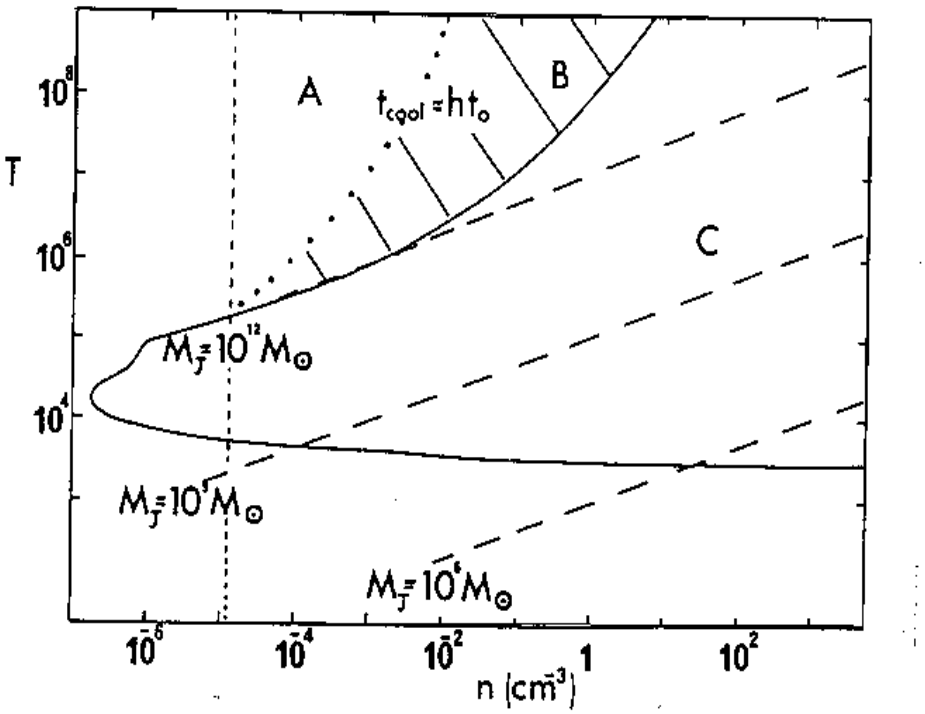

Figure 1: *The cooling diagram taken from Rees & Ostriker (1977)[47]. The $n-T$ plane is divided into three regions A, B and C. The dashed lines marked by the mass scales denote the virial relation between the temperature and the density, which are assumed to be the initial conditions of primordial gas clouds.*

Consequently, the clouds made from the density perturbations shrink as dusts and the supersonic collapse is stopped by thermal pressure at the shock front which emerge in the cloud.

The cooling diagram tells us the necessity of those clouds whose density is n and the temperature T. The $n - T$ plane is divided into three regions. Those regions are characterized by the three time scales the time scale of the Hubble expansion (τ_H), the free-fall time of the cloud (τ_{ff}) and the cooling time of the cloud (τ_{cool}). The regions are

$$A. \qquad \tau_{cool} > \tau_H, \tag{1. 1}$$

$$B. \qquad \tau_H > \tau_{cool} > \tau_{ff}, \tag{1. 2}$$

$$C. \qquad \tau_{ff} > \tau_{cool}, \tag{1. 3}$$

where

$$\tau_H = \frac{2}{3}\frac{1}{\Omega^{0.5} H_0 (1+z)^{1.5}} \tag{1. 4}$$

the ionizing photons.

$$\tau_{ff} \equiv \sqrt{\frac{3\pi}{32G\rho}} \quad (1.\ 5)$$

$$\tau_{cool} \equiv \frac{1.5nkT}{n^2\Lambda(T)} \quad (1.\ 6)$$

and $\Omega, H_0, G, \rho, n, k, T$ and $n^2\Lambda(T)$ denote the cosmological density parameter, the Hubble constant, the gravitational constant, the mass density of the cloud, the number density of the cloud, the Boltzman constant, the virial temperature of the cloud and the cooling rate per unit volume. If a shock heated and virialized cloud comes into the region A, the cloud cannot cool to contract within the age of the universe. In the region B, the cloud can cool within the Hubble time, and the contraction proceeds quasistatically. In this case, the system evolves with the cooling time. On the other hand, the cloud in the region C can cool down faster than the free-fall contraction and the system evolve with the free-fall time. The initial condition of the cloud with mass M in the $n-T$ plane is the points on the lines denoted by dashed lines. We must remark that the inclination of the line along which $M = const.$ is satisfied coincides with the inclination of the boundary which divide the region C. from B. and A. at low temperature ($T \lesssim 10^6$K). The boundary at low temperature coincide with the line $M \simeq 4 \times 10^{11} M_\odot$. This scale does not depend on the density or the temperature of the system, but just on fundamental physical constants. It is,

$$M_{RO} = {\alpha_e}^3 {\alpha_g}^{-2} (\frac{m_p}{m_e})^{1/2} m_p \quad \sim 4\times 10^{11} M_\odot, \quad (1.\ 7)$$

where m_p, m_e and α_e denote the proton mass, the electron mass and the fine structure constant, and α_g is the fine structure constant of the gravity, which is

$$\alpha_g = \frac{Gm_p^2}{\hbar c}. \quad (1.\ 8)$$

This scale seems to be one of the typical scales of galaxies. In fact, in Fig.2 various types of present day galaxies are in the region C, and the clusters of galaxies are in the region B or A. As a result, this simple treatment can give the upper limit of the mass of the galaxies. However, this treatment is not good enough to investigate the whole story of galaxy formation such as the formation of the stars inside the galaxies, the morphological types of the galaxies and the formation of active galactic nuclei which may exist at the center of every galaxy.

We must also claim that Rees & Ostriker (1977) [47] assumed the chemical composition of the primordial gas cloud is in chemical equilibrium. Because there are no metals in the primordial gas clouds, cooling processes are due to hydrogen atoms and heliums. Then, below the ionizing temperature ($T \simeq 10^4$K) the cooling rate exponentially drops, and the cloud cannot cool below 10^4K. However, the chemical equilibrium is not established in the primordial gas cloud in general. Feeded cosmologically residual electrons [41] *hydrogen molecules* are formed in a non-equilibrium way. The hydrogen molecules are the coolant above $T \sim 100$K, because of their vibrational and rotational transitions. Anyway, the non-equilibrium fraction of the hydrogen molecules is a key quantity to determine the temperature of the primordial gas clouds. The cooling due to the hydrogen molecules must be taken into account in the thermal evolution of the primordial gas cloud.

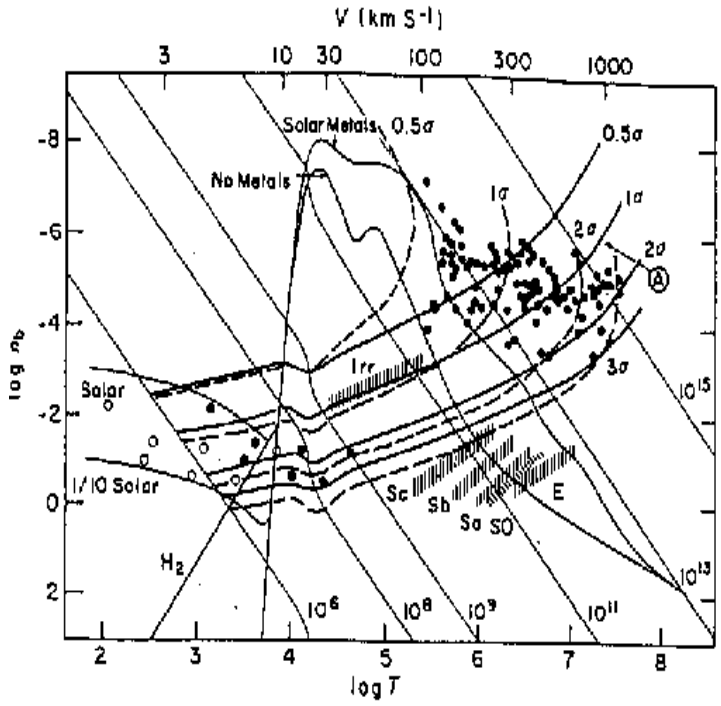

Figure 2: *The cooling diagram taken from Brumenthal et.al.(1984)[4]. Baryon density n_b versus three-dimensional r.m.s. velocity dispersion V and virial temperature T for structures of various size of the universe. The plane is divided by the cooling curve which is explained in Fig.1. Dots at upper right represent nearly all groups and clusters of galaxies within* $5000\mathrm{kms}^{-1}$ *in the CfA catalogue. The shaded regions at lower right denote the various types of galaxies. Dwarf spheroidal galaxies are plotted at lower left. The model curves denote the equilibria of structures that collapse disspationlessly from cold dark matter initial fluctuation spectra with* $n = 1$*. The solid curves and the dashed curves represent the model* $h = 0.5, \Omega = 1$ *and* $h = 1, \Omega = 0.2$ *respectively. The curves labeled* $v\sigma$ *correspond to the initial fluctuation which are* v *times greater than the r.m.s. of the fluctuations.*

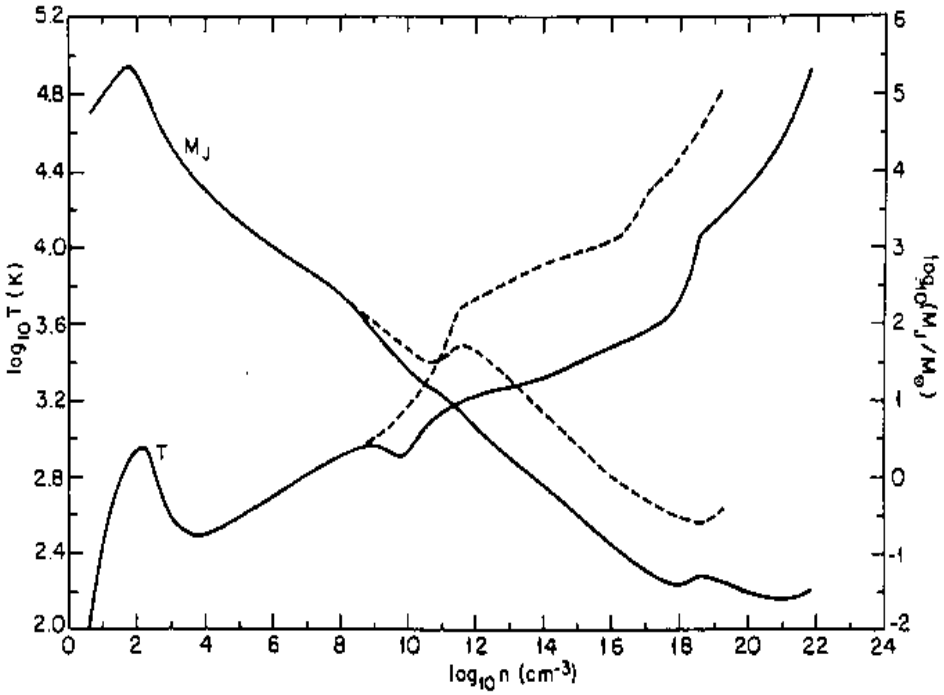

Figure 3: *The evolution of the spherically collapsing cloud in the $n-T$ plane and the evolution of Jeans mass is presented (taken from PSS [40]). There exist two local minimal Jeans mass corresponding to* H_2 *dissociation and H ionization.*

Taking into account the cooling processes by the hydrogen molecules, many authors have argued about the thermal evolution of the primordial gas clouds in pressure free collapse (Matsuda *et al.* 1969 [33]; Hutchins 1976 [20]; Carlberg 1981 [5]; Palla, Salpeter & Stahler 1983 [40](here after PSS)). As was discussed by Carlberg (1981) [5], a collapsing spherical primordial cloud has the characteristic Jeans mass scales: $20M_\odot$ at H_2 dissociation, and $0.06M_\odot$ at H ionization (Fig.3). Nevertheless, his calculation did not include the three body chemical reactions which produce hydrogen molecules, being the main coolant of the primordial gas clouds. PSS has included the three body reactions, and have shown that its Jeans mass reaches a minimum temporarily at H_2 dissociation and then drops to a true minimum value at H ionization (Fig.3), and they are smaller than those calculated in Carlberg (1981) [5]. Incidentally, these calculations were restricted to the case of the spherical clouds, though spherical clouds undergoing pressure-free collapse are unstable against non-spherical perturbation (Lin *et al.* 1965 [28]).

For such a problem related to the asphericity of the cloud, Hutchines (1976) [20] discussed that the thermal evolution of the clouds are affected greatly by the initial shape of the clouds, and their angular momentum at the initial state. Nevertheless, Hutchins (1976) [20] did not include the effect of the vibrational transitions of hydrogen molecules, and the three body reactions. If $T \gtrsim 1000$ K, H_2 the vibrational cooling rate of the

hydrogen molecules is comparable with the rotational cooling rate (e.g. Hollenbach & McKee 1979 [18]). If $n \gtrsim 10^8 \mathrm{cm}^{-3}$, H_2 formation rate through the three body reactions is so high that almost all hydrogen atoms become H_2 (PSS). This means that the cooling rate of his calculation was seriously underestimated. In the case of the spherical collapse this difference changes the thermal evolution qualitatively (PSS). In section 3, we investigate the aspherical collapse of the primordial gas cloud including the above effects by the one zone approximation. The effects of the angular momentum of the cloud is also discussed.

The asphericity and the initial coldness of the cloud cause the shock heating. The physics of a shocked primordial gas is investigated by Shapiro & Kang (1987) (here after SK) [50] for a steady shock. They found that the delay of the recombination process of hydrogen atoms compared to the cooling process leave significant amount of electrons after the temperature drops below 10^4K. The residual electrons (protons) left in the cooled postshock gas become the catalyst of H_2 formation processes,

$$\begin{aligned} \mathrm{H} + \mathrm{e} &\rightarrow \mathrm{H}^- + \gamma, \\ \mathrm{H}^- + \mathrm{H} &\rightarrow \mathrm{H}_2 + \mathrm{e}, \end{aligned}$$

and

$$\begin{aligned} \mathrm{H} + \mathrm{H}^+ &\rightarrow \mathrm{H}_2^+ + \gamma, \\ \mathrm{H}_2^+ + \mathrm{H} &\rightarrow \mathrm{H}_2 + \mathrm{H}^+. \end{aligned}$$

Hence, the hydrogen molecules are over produced and the postshock region quickly cools down to $T \sim 100$K. The dynamical and thermal evolution of the shocks which are expected in the collapsing primordial clouds are the main theme of this thesis. We reexamine the steady shock in section 5 in a different way from the one in SK. In section 6, the dynamical and thermal evolution of gravitationally collapsing clouds are studied by numerical simulations. In those calculations, non-steady shocks are expected. The mass of the fragments are also discussed in section 6.

2 Cooling processes in primordial gas cloud

Before we proceed to the collapse of primordial gas clouds, we present a brief review of cooling processes in primordial gas clouds. Compared with the interstellar medium which contains dusts and metals, primordial clouds have only light elements, and the hydrogen dominates the other species. Thus the cooling processes in primordial gas clouds are related to hydrogen atoms and hydrogen molecules.

2.1 Radiative recombination

The thermal energy loss associated with the recombination of proton with electron is caused by the photon emitted during the process. The recombined atom which is in an excited state in general, eventually decays to the lowest level with emitting a photon whose energy is equal to the energy difference between the excited state and the lowest. Accordingly, the energy loss per one recombination process is the difference between the bound states of the hydrogen atom and the kinetic energy of the free electron. The cross section of the recombination is estimated by the case B recombination. In other words, we employ the recombination rate as the summation of the rates that the electron drops to the levels except the lowest level. We use this recombination rate because the atom recombined directly to the lowest level emits the photon which is energetic enough to photoionize the nearby atom. Then the net energy loss associated with the recombination to the lowest state is negligible. The cross section of the recombination denoted as σ_{fb}(n) is,

$$\sigma_{fb}(n) = \sigma_{bf}(n)\frac{m_e^2c^2v^2}{\nu_n^2h^2+m_ev^2/2}\frac{1}{n^2}, \quad (2.\ 1)$$

where

$$\sigma_{bf}(n) = \frac{64\pi ng}{3\sqrt{3}}\alpha a_0\left(\frac{h\nu_n}{h\nu_n+m_ev^2/2}\right)^3. \quad (2.\ 2)$$

Here $\sigma_{bf}(n)$ is the photoionization cross section. $m_e, c, v, \nu_n, h, n, g, \alpha$ and a_0 denote electron mass, speed of light, the electron velocity, the frequency of an emitted photon in recombination to the nth level, Plank constant, the quantum number of the energy level, gaunt factor, fine structure constant and Bohr radius, respectively. Using the above expression, we can calculate the recombination rate by averaging the electron velocity assuming Maxwellian distribution, as

$$< \sigma_{fb}(n)v > = \int_0^\infty vf(v)\sigma_{fb}(n)dv \quad (2.\ 3)$$

$$= 3.262\times10^{-6}M(n,T), \quad (2.\ 4)$$

where

$$f(v) = 4\pi\left(\frac{m_e}{2\pi kT}\right)^{3/2}v^2\exp\left(\frac{-m_ev^2}{2kT}\right), \quad (2.\ 5)$$

Table 1: **The Recombination Function ϕ**

T [K]	ϕ	$T[10^4\mathrm{K}]$	ϕ
31.3	3.89	1.6	1.06
62.5	3.57	3.2	0.80
125	3.25	6.4	0.59
250	2.92	12.8	0.96
500	2.60	25.6	0.73
1000	2.27	51.2	0.52
2000	1.96	100	0.36
4000	1.64	1000	0.074
8000	1.34	10000	0.011

and

$$M(n,T) = \frac{e^{h\nu_n/kT}}{n^3 T^{3/2}} E_1(h\nu_n/kT). \quad (2.\ 6)$$

Here $E_1(x)$ denotes the first exponential integral. Summing up the above expression for $n \geq 2$ we obtain the recombination rate. According to Spitzer (1977) [56], the recombination rate is written in the form as,

$$k_{rec} = 2.06 \times 10^{-13} \left(\frac{T}{10^4\mathrm{K}}\right)^{-1/2} \phi(1.58 \times 10^5\mathrm{K}/T), \quad (2.\ 7)$$

where $\phi(x)$ is listed in Table 1 for different temperatures. In our calculations, we linearly interporate this table to get the recombination rate. Next we can get the cooling rate due to the recombination. Assuming the case B recombination, the cooling rate is estimated as

$$\Lambda_{rec} = n_e n_p \sum_{n\geq 2} \frac{1}{2} m_e \int_0^\infty v^3 f(v) \sigma_{fb}(n) dv. \quad (2.\ 8)$$

In our calculations, we employ the Spitzer's results again. The cooling rate is expressed as follows :

$$\Lambda_{rec} = 2.86 \times 10^{-27} n_e n_p T^{1/2} \chi(1.58 \times 10^5\mathrm{K}/T) \quad \mathrm{erg\ s^{-1}cm^{-3}}, \quad (2.\ 9)$$

where $\chi(x)$ is the function listed in Table 2 for different temperatures.

2.2 Collisional Ionization

The collisional ionization of the hydrogen atom is also a cooling process. The energy loss in this process is not responsible to the radiation emitted away, but the ionization potential energy. In other words, the thermal energy of electrons are converted to the

Table 2: **The function χ in $\sum < v^3 \sigma_{fb} >$**

T [K]	χ	T[K]	χ
31.3	3.46	2000	1.49
62.5	3.12	4000	1.20
125	2.78	8000	0.92
250	2.45	16000	0.67
500	2.12	32000	0.46
1000	1.80	64000	0.30

ionization energy in this process. The cross section of collisional ionization taken from Lotz (1968)[29] is

$$\sigma_{ion} = a_1 q_1 \frac{\ln E/P_1}{EP_1} \left(1 - b_1 \exp\left(-c_1 \left(E/P_1 - 1\right)\right)\right); \qquad E \geq P_1, . \qquad (2.\ 10)$$

where $q_1 = 1, a_1 = 4 \times 10^{-14}\mathrm{cm}^2(\mathrm{eV})^2, b_1 = 0.60, c_1 = 0.56, P_1 = 13.6\mathrm{eV}$ and E is the energy of the impact electron. The rate coefficient is obtained integrating $\sigma_{ion} v$ over the Maxwellian distribution (eqation.(2. 5)),

$$\begin{aligned} < \sigma_{ion} v > &= \int_0^\infty v f(v) \sigma_{ion} dv, & (2.\ 11) \\ &= 2.68 \times 10^{-6} \frac{1}{(kT)^{3/2}} & (2.\ 12) \\ &\times \left(\frac{1}{P_1/kT} E_1(P_1/kT) - \frac{b_1 \exp(c_1)}{P_1/kT + c_1} E_1(P_1/kT + c_1) \right) \mathrm{cm}^3\mathrm{s}^{-1}, \end{aligned}$$

where $E_1(x)$ denotes the first exponential integral, $\int_x^\infty \frac{e^{-y}}{y} dy$.

2.3 Bound-bound transition of hydrogen atom

This is the most important cooling process around $T \sim 10^4$K. Bound-bound transition of hydrogen atoms emit the radiation whose energy amount to the energy difference between the two levels. We need the transition rate between any two energy levels and the level population to estimate the cooling rate. The decay rate of the hydrogen atom at nth energy level to mth level is known as the Einstein's A coefficient. A_{nm} (A coefficient from nth level to mth) is written as,

$$A_{nm} = -\frac{8\pi^2 e^2 \nu_{nm}^2 f_{nm}}{m_e c^3}, \qquad (2.\ 13)$$

where ν_{nm} and f_{nm} denote the difference of the frequency between the two levels and the emission oscillator strength, respectively. In Table 3, A_{nm} and f_{nm} are listed (Sobelman *et.al.* 1991 [55]).

Table 3: A-**coefficients of Hydrogen Atom**

n - m	f_{nm}	A_{nm}
1 - 2	4.16×10^{-1}	$4.70 \times 10^{8}\mathrm{s}^{-1}$
1 - 3	7.91×10^{-2}	$5.57 \times 10^{7}\mathrm{s}^{-1}$
1 - 4	2.90×10^{-2}	$1.28 \times 10^{7}\mathrm{s}^{-1}$
2 - 3	6.40×10^{-1}	$4.41 \times 10^{7}\mathrm{s}^{-1}$
2 - 4	1.19×10^{-1}	$8.42 \times 10^{6}\mathrm{s}^{-1}$
3 - 4	8.42×10^{-1}	$8.99 \times 10^{6}\mathrm{s}^{-1}$

It is shown that the Lyman-α line has much larger transition rate than the other lines in this table. In fact, around $T \sim 10^4$K, Lyman-α line cooling dominates the total cooling rate. The level population of hydrogen atoms is determined by the balance equation of the excitation rate and the de-excitation rate between the levels. In our calculations, the de-excitation rate is dominated by the radiative transition from the higher level to the lower because the density of the cloud is sufficiently low. The excitation is controlled by the collisional excitation. As a result, the balance equations are,

$$\sum_{n>m} A_{nm} n_n + \sum_{n<m} C_{nm} n_n n_e = \sum_{n<m} A_{mn} n_m + \sum_{n>m} C_{mn} n_m n_e, \qquad (2.\ 14)$$

where n_m and C_{nm} denote the number density of hydrogen atoms at nth level and the collisional excitation rate from nth level to mth. The collisional excitation rate $C_{nm} = <\sigma_{nm} v>$ is taken from Sobelman et.al.(1977) [54]. According to their book, the collisional excitation rate is expressed as,

$$C_{nm} = 10^{-8} \left(\frac{13.6eV}{h\nu_n - h\nu_m} \right)^{3/2} \left(\frac{\nu_m}{\nu_n} \right)^{3/2} \frac{1}{n} e^{-\beta} G(\beta) \quad \mathrm{cm}^3\mathrm{s}^{-1}, \qquad (2.\ 15)$$

where

$$\beta = (h\nu_n - h\nu_m)/kT, \qquad (2.\ 16)$$

and

$$G(\beta) = A \frac{\sqrt{\beta(\beta+1)}}{\beta + \chi}. \qquad (2.\ 17)$$

A and χ are given in Table 4. The cooling rate is expressed as,

$$\Lambda = \sum_{n \geq 2} \sum_{m<n} A_{nm} n_n. \qquad (2.\ 18)$$

Here we must remark one important point below. The cloud that we treat has the scale of galaxies. As a consequence, the cloud is highly optically thick at Lyman photon frequency, although we treat the cooling function as if the cloud is optically thin in equation (2. 18).

Table 4: **The Parameters in the Cross Section of Collisional Excitation**

n - m	A	χ
1 - 2	24	0.28
1 - 3	22	0.37
1 - 4	22	0.39
2 - 3	67	0.30
2 - 4	58	0.45
3 - 4	124	0.26

However, the energy density of maximally emitted Lyman-α photons from hydrogen atoms is lower than the 'heat capacity' of photons at $T \sim 10^4$K. In other words, the space is not 'filled' with radiation though the system is highly optically thick. The capacity [cm^{-3}] for the Lyman-α photons are,

$$N_{cap} \simeq \frac{4\pi B_\nu(T)\Delta\nu}{ch\nu}, \tag{2. 19}$$

where

$$B_\nu(T) = \frac{2h\nu^3/c^2}{\exp(h\nu/kT)-1}, \tag{2. 20}$$

and $\Delta\nu$ denotes the Doppler broading of the line. The maximal number density of Lyman-α photons emitted from the gas particles is estimated as follows: Once the cloud heated up to high temperature, say $T \gtrsim 10^5$K, many Lyman photons are produced through the collisional excitation process of neutral atoms. However, the Lyman photons can escape from the cloud because the cloud is highly ionized at this temperature. That is why the Lyman photons excited at high temperature are not trapped in the cloud. When the cloud cools down to the temperature $\sim 10^4$K, the neutral fraction of hydrogen atoms increase. As a consequence, the cloud becomes highly optically thick, and the Lyman photons are trapped in the cloud. On the other hand, the energy density of Lyman α photons trapped in the cloud is bounded by the thermal energy density of the gas particles at $T \sim 10^4$K. Comparing this maximal number density of the Lyman α photons with the photon capacity of the space (eq.(2. 19)),

$$\frac{N_{max}}{N_{cap}} \simeq \frac{3/2 n_H kT}{h\nu}\frac{ch\nu}{4\pi B_\nu(T)\Delta\nu}, \tag{2. 21}$$

$$= \frac{3/2 n_H ckT}{4\pi B_\nu(T)\Delta\nu}, \tag{2. 22}$$

The ratio N_{max}/N_{cap} is drawn as a function of temperature in Fig.4. It is shown that the ratio is smaller than unity for $T \gtrsim 10^4$K at which the Lyman α cooling is the most important process.

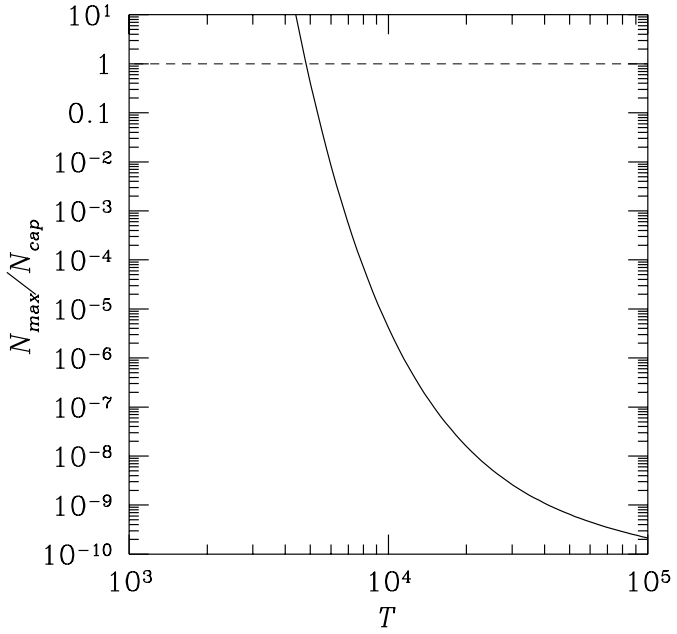

Figure 4: *The ratio in equation (2. 22) is presented for* $n_H = 10^2\mathrm{cm}^{-3}$. *The ratio is smaller than* 1 *for* $T \gtrsim 10^4\mathrm{K}$ *at which the Lyman* α *cooling is the most important process.*

2.4 Thermal bremsstrahlung emission

Radiation due to the acceleration of a charge in Coulomb field of another charge is called bremsstrahlung or free-free emission. The energy emitted from the encounter of a proton with a single-speed electron is expressed as [49],

$$\frac{dE}{d\nu dV dt}(v,\nu) = \frac{16\pi e^6}{3\sqrt{3}c^3 m_e^2 v} n_p n_e g_{ff} \quad \text{erg s}^{-1}\text{cm}^{-3}\text{Hz}^{-1}, \tag{2. 23}$$

where v, ν, and g_{ff} denote the velocity of primary electron, the frequency of the emitted radiation and the gaunt factor of free-free emission. Now averaging equation (2. 23) over the velocity with equation 2. 5 we obtain the emissivity of the thermal bremsstrahlung radiation. Performing the integral

$$\frac{dE}{dV dt d\nu}(T,\nu) = < \frac{dE}{dV dt d\nu}(v,\nu) > \tag{2. 24}$$

$$= \int_{v_{min}}^{\infty} \frac{dE}{dV dt d\nu}(v,\nu) f(v) dv, \tag{2. 25}$$

where $v_{min} \equiv \sqrt{2h\nu/m_e}$, and we obtain

$$\frac{dE}{dV dt d\nu} = \frac{32\pi e^6}{3m_e c^3}\left(\frac{2\pi}{3km_e}\right)^{1/2} T^{-1/2} n_e n_p \exp\left(-h\nu/kT\right) < g_{ff} > . \tag{2. 26}$$

The lower bound of the integral v_{min} comes out of the fact that the incident kinetic energy must be above the radiated energy. The cooling rate is estimated by intergrating again the eqation (2. 26) over the frequency. Performing the integral,

$$\Lambda_{ff} = \int_0^\infty \frac{dE}{dVdtd\nu}(T,\nu)d\nu, \tag{2. 27}$$

we obtain

$$\Lambda_{ff} = 1.426 \times 10^{-27} n_e n_p T^{1/2} < g_{ff} > \quad \text{erg s}^{-1}\text{cm}^{-3}, \tag{2. 28}$$

where $< g_{ff} >$ is the averaged gaunt factor, which obeys the following empirical formula:

$$< g_{ff} > = 0.79464 + 0.1243 \log T \quad \text{for} \quad T < 3.2 \times 10^5 \text{K}, \tag{2. 29}$$

$$= 2.13164 - 0.1240 \log T \quad \text{for} \quad T > 3.2 \times 10^5 \text{K}. \tag{2. 30}$$

2.5 H_2 radiative cooling (optically thin limit)

The process of H_2 radiative cooling is very important for the primordial gas at rather low temperature ($T \lesssim 10^4$K). The hydrogen molecules have the energy levels corresponding to the vibrational transitions and the rotational transitions. The vibrational transitions are more important at high temperature ($10^3 K \lesssim T \lesssim 10^4$K) , and the others are more significant at low temperature ($T \lesssim 10^3$K). The estimation of the cooling rate is done in the same way as the case of atomic bound-bound transitions. However we must remark that the situation is different from that of the atomic line cooling process. First of all, the 'photon capacity' is much smaller than the previous case, because the capacity is proportional to T^3 and the temperature is lower than 10^4K, when the molecular line cooling is effective. Accordingly, we must treat the radiative transfer of molecular line photons carefully. Secondly, the Einstein's A-coefficients are extremely smaller than the previous case, because the hydrogen molecules have no dipole moments. As a result, the absorption coefficient become much smaller and the critical column density above which the cloud is optically thick become much larger. The small A-coefficients also affect the level population of the excited states. The collisional de-excitation process is effective for $n \gtrsim 10^4\text{cm}^{-3}$ though the critical density for hydrogen atom is higher than 10^{15}cm^{-3}. When the cloud is optically thick, we have to solve the level populations to estimate the emissivity and the radiative transfer equation for each line (Appendix A). However in case the cloud is optically thin, the fitting formulae are already given by several authors. We use the one presented by Hollenbach and McKee (1979) [18]. According to their paper, the cooling function is expressed as

$$\Lambda_{\mathrm{H}_2 vr} = n_{\mathrm{H}_2}(n_{\mathrm{H}} L_{vr}^{\mathrm{H}} + n_{\mathrm{H}_2} L_{vr}^{\mathrm{H}_2}), \tag{2. 31}$$

$$\mathrm{L}_{vr}^{\mathrm{H},\mathrm{H}_2} = \frac{L_r^{\mathrm{H},\mathrm{H}_2}(n \to \infty)}{L_r^{\mathrm{H},\mathrm{H}_2}(n \to \infty) + L_r^{\mathrm{H},\mathrm{H}_2}(n \to 0)} + \frac{L_v^{\mathrm{H},\mathrm{H}_2}(n \to \infty)}{L_v^{\mathrm{H},\mathrm{H}_2}(n \to \infty) + L_v^{\mathrm{H},\mathrm{H}_2}(n \to 0)} \tag{2. 32}$$

where

$$L_r^{\mathrm{H},\mathrm{H}_2}(n \to \infty) = \frac{1}{n_{\mathrm{H},\mathrm{H}_2}} \tag{2. 33}$$

$$\times \left(\left(\frac{9.5 \times 10^{-22} T_3^{3.76}}{1 + 0.12 T_3^{2.1}} \right) e^{-(0.13/T_3)^3} + 3 \times 10^{-24} e^{-(0.51/T_3)} \right),$$

$$L_v^{\rm H,H_2}(n \to \infty) = \frac{1}{n_{\rm H,H_2}} \left(6.7 \times 10^{-19} e^{-(5.86/T_3)} + 1.6 \times 10^{-18} e^{-(11.7/T_3)} \right), \quad (2.\ 34)$$

$$L_r^{\rm H,H_2}(n \to 0) = 0.25 \left(5 \gamma_2^{\rm H,H_2} \left(E_2 - E_0 \right) e^{-\frac{E_2 - E_0}{kT}} \right)$$

$$+0.75 \left(\frac{7}{3} \gamma_3^{\rm H,H_2} \left(E_3 - E_1 \right) e^{-\frac{E_3 - E_1}{kT}} \right), \quad (2.\ 35)$$

$$L_r^{\rm H,H_2}(n \to 0) = \gamma_{10}^{\rm H,H_2} e^{-\frac{E_{10}}{kT}} + \gamma_{20}^{\rm H,H_2} e^{-\frac{E_{20}}{kT}}, \quad (2.\ 36)$$

with

$$\gamma_J^{\rm H_2} = \left(\frac{1 \times 10^{-11} T_3^{1/2}}{1 + 60 T_3^{-4}} + 1 \times 10^{-12} T_3 \right) \left(0.33 + 0.9 e^{-\left(\frac{J - 3.5}{0.9} \right)^2} \right), \quad (2.\ 37)$$

$$\gamma_J^{\rm H_2} = \left(3.3 \times 10^{-12} + 6.6 \times 10^{-12} T_3 \right) \left(0.276 J^2 e^{-\left(\frac{J}{3.18} \right)^{1.7}} \right), \quad (2.\ 38)$$

$$\gamma_{10}^{\rm H} = 1 \times 10^{-12} T^{1/2} \exp\left(-(1000/T) \right), \quad (2.\ 39)$$

$$\gamma_{20}^{\rm H} = 1.6 \times 10^{-12} T^{1/2} \exp\left(-(400/T)^2 \right), \quad (2.\ 40)$$

$$\gamma_{10}^{\rm H_2} = 1.4 \times 10^{-12} T^{1/2} \exp\left(-(12000/\left(T + 1200 \right))^2 \right), \quad (2.\ 41)$$

$$\gamma_{20}^{\rm H_2} = 0, \quad (2.\ 42)$$

$$T_3 \equiv T/1000{\rm K}, \quad (2.\ 43)$$

$$(E_2 - E_0)/k = 512{\rm K}, \quad (2.\ 44)$$

$$(E_3 - E_1)/k = 845{\rm K}, \quad (2.\ 45)$$

$$E_{10}/k = E_{20}/2k = 5860{\rm K} \quad (2.\ 46)$$

Here, $L^{\rm H,H_2}$ and $\gamma^{\rm H,H_2}$ denote the value $L^{\rm H}, L^{\rm H_2}$, and $\gamma^{\rm H}, \gamma^{\rm H_2}$ respectively. The units of all L and γ are erg ${\rm s^{-1}cm^3}$ and ${\rm cm^3 s^{-1}}$, respectively. In the above expression, $\Lambda_{{\rm H_2}vr}$ consists of two parts. The first term is the contribution from the ${\rm H - H_2}$ collisional excitation and the second is due to the ${\rm H_2 - H_2}$ collisional excitation. We also find that $L_r^{\rm H,H_2}$ and $L_v^{\rm H,H_2}$ have the two limiting values for $n \to \infty$ and $n \to 0$. The dependence of these limiting values on the density are different from each other. The former are proportional to n^{-1} and the latter are independent of the density. The difference is due to the dependence of the fraction of the excited hydrogen molecules on the density. The level population are determined by the balance between the de-excitation rates from higher levels to lower levels and the excitation rates. The excitation rates are always dominated by the collisional excitation processes, though the de-excitation rates are determined by both the collisional processes and the radiative ones. The collisional de-excitation rates are proportional to n^2 and the radiative decay rates are proportional to n. Accordingly, the de-excitation rates are dominated by the collisional process at high density, and the radiative decay dominates the de-excitation process for low densiy. As a result, the number density of excited molecules are proportional to n^2 at low density and to n at high density. The emissivity $(n^2 L)$ is the

product of the number density of the excited molecules and the radiative transition rates. Therefore, the limiting values $L(n \to \infty)$ and $L(n \to 0)$ in equation (2. 32) have different dependence on density. The density at which the collisional excitation rates equal to the radiative decay rates is called the *critical density* and its value is $\sim 10^4 \mathrm{cm}^{-3}$ for the lowest rotational transition. The fitting formulae in equation (2. 31) and (2. 32) include these effects and also well fit around the critical density.

2.6 H_2 dissociation

Hydrogen molecules have lower potential energy than the state of two separated neutral hydrogens. Then the dissociation of hydrogen molecules absorb the thermal energy of the other particles which collide with hydrogen molecules causing the dissociation. Then, the cooling rate is given as

$$\Lambda_{diss} = 7.16 \times 10^{-12} \left(\frac{dn(\mathrm{H}_2)}{dt} \right)_{-} \quad \mathrm{erg\ s^{-1} cm^{-3}}, \tag{2.47}$$

where $n(\mathrm{H}_2)$ denotes the number density of hydrogen molecules. In the above equation, $(dn(\mathrm{H}_2)/dt)_{-}$ is the dissociation rate of H_2 (SK [50]). The time variation of the fraction of any species is given at each time step in our calculations, because we solve the time dependent rate equations coupled with the energy equation.

The reaction rate coefficients which should be used to estimate $\left(\frac{dn(\mathrm{H}_2)}{dt}\right)_{-}$ is taken from SK. The dissociation processes of hydrogen molecules have three channels, which are H_2-H^+ collision (k_{12}), H_2-H collision (k_5)and H_2-H_2 collision (k_7)[2]. The first channel is efficient when the system is highly ionized. The rate coefficient of this chanel is presented in table 9. The latter two channels are important when the system have low ionization degree. The reaction rates are expressed as,

$$k_5 = k_{H5}^{\frac{1}{1+n_{cr5}/n_N}} k_{L5}^{\frac{1}{1+n_N/n_{cr5}}}, \tag{2. 48}$$

$$k_7 = k_{H7}^{\frac{1}{1+n_{cr7}/n_N}} k_{L7}^{\frac{1}{1+n_N/n_{cr7}}}, \tag{2. 49}$$

where,

$$n_{cr5} = \mathrm{dex}4.0 - 0.416 \log T/10^4 - 0.327(\log(T/10^4))^2 \quad \mathrm{cm^{-3}}, \tag{2. 50}$$

$$n_{cr7} = \mathrm{dex}4.845 - 1.3 \log T/10^4 + 1.62(\log(T/10^4))^2 \quad \mathrm{cm^{-3}}, \tag{2. 51}$$

$$k_{L5} = 1.12 \times 10^{-10} \exp\left(-7.035 \times 10^4/T\right) \quad \mathrm{cm^{-3}}, \tag{2. 52}$$

$$k_{L7} = 1.18 \times 10^{-10} \exp\left(-6.95 \times 10^4/T\right) \quad \mathrm{cm^{-3}}, \tag{2. 53}$$

$$k_{H5} = 1.20 \times 10^{-9} \exp\left(-5.24 \times 10^4/T\right) \quad \mathrm{cm^{-3}}, \tag{2. 54}$$

$$k_{H7} = 1.30 \times 10^{-9} \exp\left(-5.33 \times 10^4/T\right) \quad \mathrm{cm^{-3}}. \tag{2. 55}$$

2.7 H_2 formation

The H_2 formation process is essentially the opposite to the H_2 dissociation process. The hydrogen molecules are in an excited state when they form. Hence, if the subsequent

[2] k_is denote the reaction rate coefficients which are listed in table 9

collisional de-excitation process is dominant compared to the spontaneous decay process, the excitation energy is transported into the thermal energy of electrons. If the spontaneous decay rate is greater than the collisional de-excitation rate, the energy is radiated away (H_2 line emission) and this process does not help to heat the gas cloud. We take into account this correction which should be adopted to Λ_{diss}. According to SK[50], the heating rate is expressed as

$$\Gamma_{form} = 7.16 \times 10^{-12} \left(\frac{dn(\mathrm{H}_2)}{dt} \right)_+ \frac{1}{1 + n_{cr}/n_H} \text{ erg s}^{-1}\text{cm}^{-3}, \tag{2.56}$$

where n_H denotes the total number density of hydrogen nuclei, $(dn(\mathrm{H}_2)/dt)_+$ is the formation rate of H_2, and n_{cr} is the critical density which is defined as follows:

$$n_{cr} = \frac{10^6}{\sqrt{T} n_H} \left(1.6 \exp\left(-\left(\frac{500}{T} \right)^2 \right) n(\mathrm{H}) + 1.4 \exp\left(-\frac{12000}{T + 1200} \right) n(\mathrm{H}_2) \right). \tag{2.57}$$

In the above equation, $(1 + n_{cr}/n_H)^{-1}$ is the correction term, due to the spontaneous decay of excited levels.

3 The one zone collapse model : non-spherical collapse of the primordial gas clouds

Following the works by PSS and Hutchines, Susa et.al.(1996)[57] investigated the non-spherical collapse of the primordial gas clouds including the vibrational transition of hydrogen molecules and the three body reactions those are not taken into account by Hutchines.

3.1 Density evolution of the cloud

We regard the evolution of the gas cloud to be dust collapse. This assumption is justified, if the free-fall time $t_{grav} \sim (G\rho)^{-1/2}$ is much shorter than the sound crossing time. In our calculation, this condition always holds. We also assume the cloud to be homogeneous for simplicity. If we consider spherical collapse, the evolution of the density is easily determined by one equation of motion. However, we are interested in non-spherical collapse of the cloud. We take into account the non-sphericity by using the collapse of a uniform spheroid as was introduced by Lin *et al.* (1965) [28] and Hutchins (1976) [20]. According to Hutchins(1976) [20], the spheroidal collapse with angular momentum can be described as,

$$\frac{d^2R}{d\tau^2} = -\alpha_0 F(\alpha) R^{-2} + \xi R^{-3}, \tag{3. 1}$$

$$\frac{d^2Z}{d\tau^2} = -{\alpha_0}^{-1} G(\alpha) R^{-1} Z^{-1}, \tag{3. 2}$$

$$\rho = \rho_0 R^{-2} Z^{-1}, \tag{3. 3}$$

where R and Z are respectively the radial and axial sizes of the cloud normalized by the initial size. Also other variables or functions are as follows:

$$r \equiv r_0 R, \tag{3. 4}$$

$$z \equiv z_0 Z, \tag{3. 5}$$

$$\alpha_0 \equiv z_0/r_0, \tag{3. 6}$$

$$\alpha \equiv z/r = \alpha_0 Z/R, \tag{3. 7}$$

$$\tau \equiv t/(4\pi G\rho_0)^{-1/2}, \tag{3. 8}$$

$$\xi \equiv \left(\omega_0 (4\pi G\rho_0)^{-1/2}\right)^2, \tag{3. 9}$$

where, r_0 and z_0 are the initial physical sizes of the cloud, ρ_0 is the initial density, t denotes the elapsing time from the beginning of the collapse, and ω_0 is the initial angular velocity of the cloud. The definitions of two functions $F(x)$ and $G(x)$ are given as

$$F(x) \equiv \frac{\arccos(x) - x\sqrt{(1-x^2)}}{2(1-x^2)^{3/2}}, \tag{3. 10}$$

$$G(x) \equiv \frac{-x^2 \arccos(x) + x\sqrt{(1-x^2)}}{(1-x^2)^{3/2}}, \tag{3. 11}$$

for $x < 1$, and

$$F(x) \equiv \frac{\ln(x+\sqrt{x^2-1}) - x\sqrt{x^2-1}}{2(x^2-1)^{3/2}}, \tag{3. 12}$$

$$G(x) \equiv \frac{-x^2\ln(x+\sqrt{x^2-1}) + x\sqrt{x^2-1}}{(x^2-1)^{3/2}}, \tag{3. 13}$$

for $x > 1$.

Equations (3.1) and (3.2) are solved numerically, with the initial conditions,

$$R(0) = Z(0) = 1, \tag{3. 14}$$

$$\frac{dR}{d\tau} = \frac{dZ}{d\tau} = 0. \tag{3. 15}$$

These initial conditions are set at the maximal expansion epoch of the density perturbations.

3.2 Thermal evolution and chemical reactions

Here we show the energy equation and the cooling functions. We also summarize the reaction rates for five compositions of primordial gas clouds, which we take into account for the calculations.

First of all, the following is the energy equation which we solve:

$$\frac{d\epsilon}{dt} = p(T,\rho)\frac{d\,(1/\rho)}{dt} - \Lambda(\rho,T), \tag{3.16}$$

where ϵ, p and ρ denote the internal energy per unit mass, the pressure of the gas cloud, and the density of the cloud, respectively. The first term on the right-hand side of the above equation denotes the adiabatic heating/cooling, and the second term, Λ, denotes the cooling rate or heating rate due to various physical processes excluding the adiabatic change. We also use the equation of state for an ideal gas.

In the cooling function we take into account the H_2 vibrational and rotational line cooling, as well as the heating and the cooling due to the H_2 formation and dissociation (section 2, Appendix A). We also solve the radiative transfer equation to evaluate the radiative cooling properly. To obtain the overall radiative energy loss from the cloud, we calculate the net flux radiated from the surface of the cloud (Appendix B). Then, we estimate the radiative cooling rate per unit mass of the cloud.

The reaction rates are taken from Table 1 of PSS. The chemical compositions which we introduced in the present calculation are e^-, H^+, H, H^-, H_2. We exclude helium for simplicity, since helium plays an important role only at high temperature ($T \gtrsim 10^5$K).

3.3 Initial conditions

Now we can calculate the thermal evolution of the collapsing gas clouds under a given set of initial conditions. In this paper, we set the mass of the cloud to be $10^6 M_\odot$, which is consistent with the Jeans mass just after the recombination. We set other physical

quantities as $\rho_0 = 4.6 \times 10^{-24}\mathrm{gcm}^{-3}$, $T_0 = 10^2\mathrm{K}$, $f_e = f_{\mathrm{H}^+} = 2.8 \times 10^{-5}$, $f_{\mathrm{H}^-} = 3.0 \times 10^{-12}$ and $f_{\mathrm{H}_2} = 6.3 \times 10^{-6}$, respectively. Here ρ_0, T_0 and f_X denote the initial density, the initial temperature, and the number fraction of the composition X, respectively. For comparison, we have chosen the same values as PSS, which are also close to those used by Hutchins (1976) [20]. Then, we have two free parameters for the calculations, α_0 and ξ, α_0 being the flatness of the initial spheroid and ξ being the ratio of the rotation energy to the gravitational energy of the cloud. We show the results for different values of these two parameters, in subsection 3.5.

3.4 The limit of the calculation

The dynamical equations (3.1) and (3.2), which we introduced to solve this problem, do not contain the thermal pressure force. In other words, if the condition

$$(4\pi G\rho)^{-1/2} \quad = min(r,z)/c_s, \tag{3. 17}$$

is satisfied, our dynamical equations break down. This is the limit of our calculation. Then, at this time we stop our calculation.

3.5 Thermal history of the collapse

3.5.1 The collapse of the non-rotating clouds : $\alpha_0 \neq 1, \xi = 0$

The collapse of a non-rotating spheroid can be divided into two types, according to their initial conditions.

First, the collapse of an initially oblate cloud is very different from that of a spherical one, as shown by Hutchins (1976) [20]. The non-spherical collapse at the initial phase is immediately followed by a disklike collapse within a different time scale from a spherical collapse. Strictly speaking, the time needed for ρ to become infinite, is not much different from that of a spherical collapse, but *at the same density*, which is much higher than the initial value, the time scales simply determined by the temporal shrinking rates are entirely different from each other, as

$$t_{dyn} \equiv -r/v_r = \left(3\rho/\frac{d\rho}{dt}\right) \quad \propto \quad \rho^{-1/2}(\mathrm{sphere}), \tag{3. 18}$$

$$\equiv \quad -z/v_z = \left(\rho/\frac{d\rho}{dt}\right) \quad \propto \quad \rho^{-1}(\mathrm{sheet}). \tag{3. 19}$$

Because of the thinness of the disk, t_{dyn} of sheet like collapse is much smaller than the free-fall time at the same density. This time scale, t_{dyn}, is also the time scale of adiabatic heating. Consequently, the thermal evolution of these oblate spheroids is also very different from that of spherical clouds. The difference is shown in Fig.5, which is essentially the same as Hutchins (1976) [20]. Then we can conclude that in sheet-like collapse, the three body reactions are not important for the thermal history of the cloud. In other words, the temperature of the cloud rises so fast that the density cannot rise to the critical density

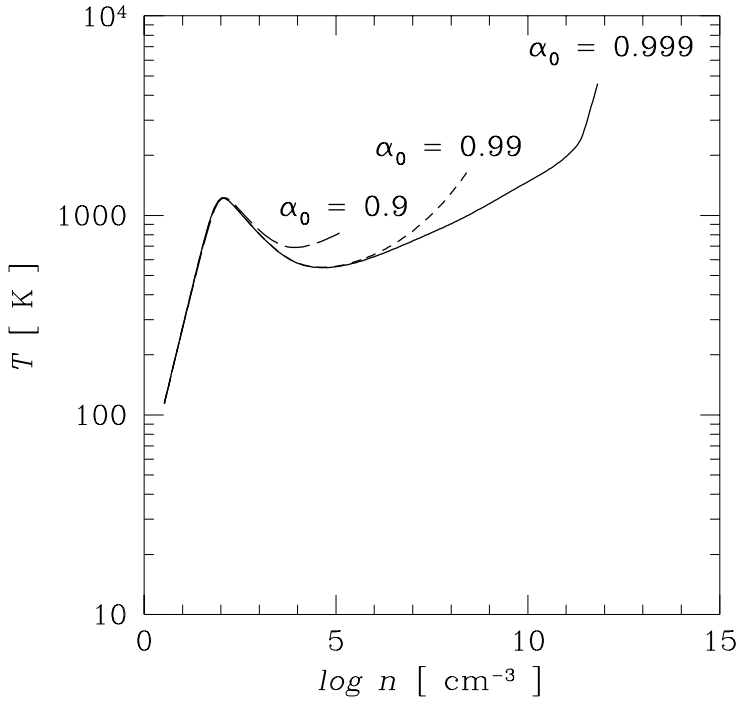

Figure 5: *The thermal evolution of the initially oblate clouds on the $n-T$ plane. Three lines are corresponding to the initial oblateness, $\alpha_0 = 0.9, 0.99$ and 0.999.*

($\sim 10^8 \mathrm{cm}^{-3}$), which is sufficient for the three body reactions to become a main contributor of producing hydrogen molecules. [3]

Second, the collapse of an initially prolate cloud (Fig.6) is not so different from that of the spherical one, because they have almost the same collapsing time scale. For a cylinder, the time scale

$$t_{dyn} \propto \rho^{-1/2}(\ln\rho)^{-1/2}(\mathrm{cylinder}), \qquad (3.\ 20)$$

is not so different from that of the spherical one, that the thermal evolution of the non-rotating prolate cloud is very similar to that of the spherical cloud. The only difference between the two cases is the critical value of the density, above which the cloud is opaque to the line emission by H_2, where the optical depth is defined in Appendix B. In the case of prolate collapse, this density is larger than the spherical case, because of its shape.

Accordingly, the three body reactions are important in this case. However, the cloud shape turns out to be a cylinder, different from the spherical case.

3.5.2 The collapse of rotating clouds

Initially spherical rotator : $\alpha_0 = 1, \xi \neq 0$

[3] Of course, sufficiently small $1-\alpha_0$ provides the opposite results, but the value α_0 need to be extremely close to unity, say 0.9999.

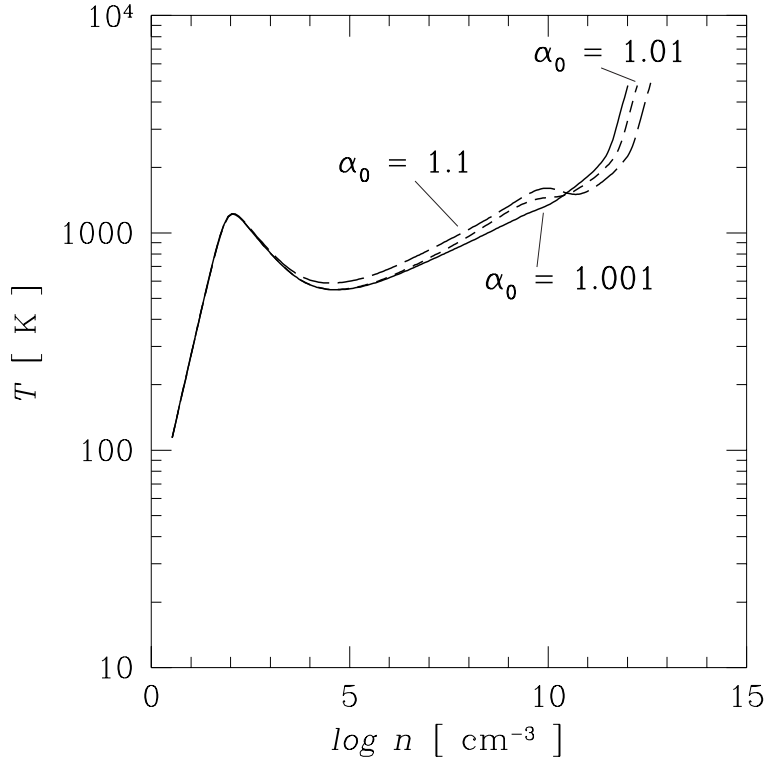

Figure 6: *The thermal evolution of the initially prolate clouds on the $n-T$ plane. Three lines are corresponding to the initial prolateness,* $\alpha_0 = 1.1, 1.01$, and 1.001.

We are also interested in the effects of angular momentum. To distinguish its effects from that of the initial shape of the cloud, we test the model of an initially spherical rotator (Fig.7) The initially spherical rotator experiences two phases during its free-fall collapse.

First, the cloud collapses spherically, because of its initial configuration. When the size of the cloud shrinks enough for the angular momentum barrier to stop the radial infall of the gas, the shape becomes disk like. Then in this second phase, eqs. (3.18),(3.19) show that the dynamical time scale is shorter than in the spherical case at the same density. What is more, this time scale is much shorter than the cooling time scale in our calculation. Accordingly, the epoch at which the type of the collapse switches from spherical type to disk like one has a significant importance on the later thermal evolution of the cloud. For example, the three body reactions,

$$3\mathrm{H} \rightarrow \mathrm{H}_2 + \mathrm{H}, \tag{3. 21}$$

$$2\mathrm{H} + \mathrm{H}_2 \rightarrow 2\mathrm{H}_2, \tag{3. 22}$$

have larger reaction rates for larger density. These reaction rates exceed the two body reaction rates for $n \gtrsim 10^8 \mathrm{cm}^{-3}$. However, when the cloud shrinks disk like and the temperature increases almost adiabatically during $n \lesssim 10^8 \mathrm{cm}^{-3}$, the collapse will be stopped by the thermal pressure before the three body reactions become effective. This situation is realized for large angular momentum. On the other hand, if the collapse

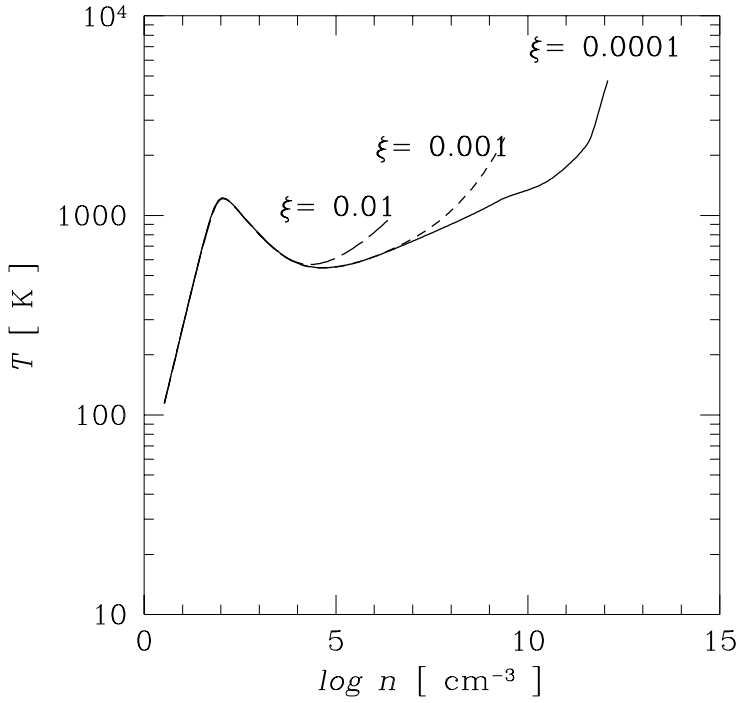

Figure 7: *The thermal evolution of the initially spherical clouds with some angular momentum on the $n-T$ plane. Three lines are corresponding to the magnitude of the initial angular momentum, $\xi = 0.01, 0.001$ and 0.0001.*

proceeds spherically during $n \lesssim 10^8 \mathrm{cm}^{-3}$, the three body reactions could play important roles before the cloud is stopped by the thermal pressure.

We can find the critical value of the rotation parameter ξ which is sufficiently small that the three body reactions become important for the formation of hydrogen molecules. This critical value of ξ is roughly obtained by the following estimate. According to the eqs. (3.1),(3.2), R_{sw}, the radius when the collapse type switches from spherical collapse to disk like one is simply determined as $R_{sw} = \xi$. Then, using the mass conservation law for the spherical collapse, the corresponding density is determined as $n_{sw} R_{sw}^3 = n_{sw} \xi^3 = n_0$. Finally, we can obtain the critical value of ξ from the equation $n_{sw} \simeq n_{3b}$, where n_{3b} is the critical density above which the three body reaction rates exceed the two body reaction rates. Substituting n_0 for $1\mathrm{cm}^{-3}$ and n_{3b} for $10^{-8}\mathrm{cm}^{-3}$, We obtain $\xi \sim 10^{-3}$. Actually in Fig.8, the maximum fraction of H_2 for different value of ξ is suddenly changed at $\xi \sim 10^{-4} - 10^{-3}$. But the hydrogen molecules, produced through these three body reactions, cannot radiate the thermal energy away from the cloud freely because of the absorption by itself. In other words, the rapid increase of the hydrogen molecules causes the rapid increase of the optical depth of the line emission of H_2. As a consequence, the effect of three body reactions are not very important as for the energetics of the gas cloud. Of course, this situation is different if the mass scale of the cloud is much smaller than

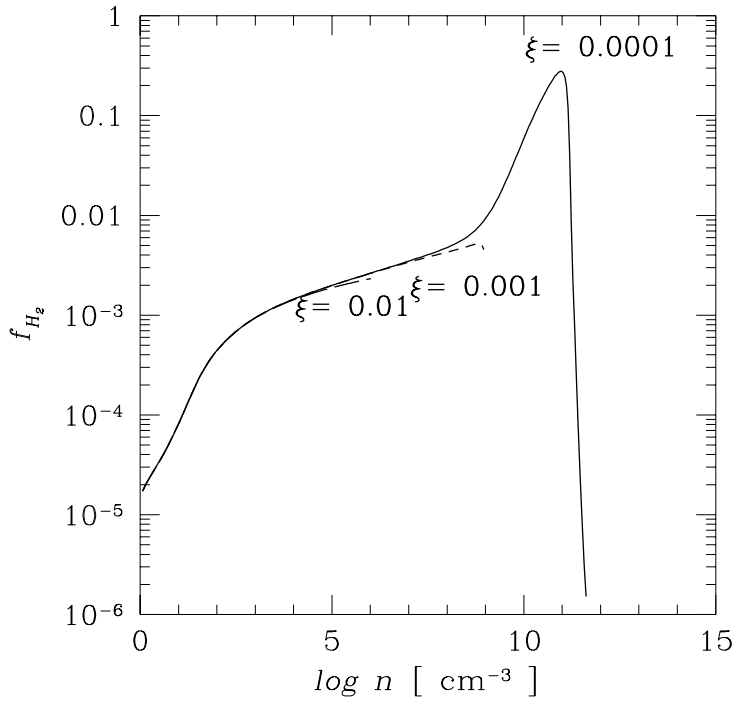

Figure 8: *The H_2 fraction of the initially spherical clouds with some angular momentum on the $n-T$ plane. Three lines are corresponding to the magnitude of the initial angular momentum, $\xi = 0.01, 0.001$ and 0.0001.*

$10^6 M_\odot$.

We can also mention that this value is very close to the cosmological value of ξ ($\simeq 10^{-4} \sim 10^{-3}$), originated from the tidal interactions among the density perturbations during their linear phase. Many authors have discussed the order of magnitude of the cosmological spin parameter λ being almost equal to 0.03 (e.g. Eisenstein & Loeb 1995 [14]). We can easily check the relation between λ and ξ is $\lambda \simeq \sqrt{\xi}$. This value is obtained for much larger mass scale than $10^6 M_\odot$, which we are interested in now, but many results support that λ is almost independent of the mass scale (Eisenstein & Loeb 1995 [14] see also references there in) . This means the possibility that the angular momentum of the cloud can be an essential parameter which determines the fragment mass.

Initially non-spherical rotator : $\alpha_0 \neq 1, \xi \neq 0$

Here we will show the thermal evolution of an initially non-spherical rotator. These results can be explained as combined results of the above two subsections. In the case of initially oblate rotator, with some realistic values of initial oblateness ($\alpha_0 \sim 0.9$) (Bardeen et.al. 1985 [1]) and of angular momentum ($\xi \sim 10^{-3}$), the cloud completes its collapse before the angular momentum barrier prevents the gas from radially collapsing. Therefore the essential parameter is not ξ, but α_0 in this case.

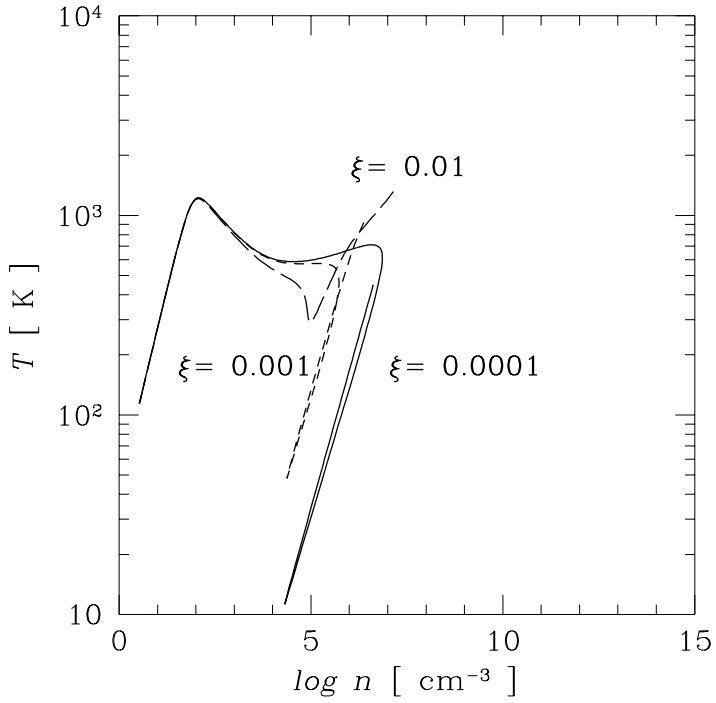

Figure 9: *The thermal evolution of the initially prolate clouds with some angular momentum on the $n-T$ plane. The initial flatness, α_0 is* 1.1*, and three lines are corresponding to the magnitude of the initial angular momentum, $\xi = 0.01, 0.001$* and *0.0001.*

ξ is an essential parameter, because of the faster collapse in the radial direction than the z-direction. The gas falling in the radial direction inevitably encounters the angular momentum barrier and then bounces. The bounced cloud is adiabatically cooled in the beginning, then recollapses to be adiabatically heated. When the cloud recollapsed to the density at which it bounced before, the shape of the cloud is no more prolate, but oblate. Then the cloud collapses to a disk, immediately followed by the end of the calculation.

3.6 The mass of the fragments

We estimate the mass of the fragments as follows. For example, in the case of initially spherical rotator, the evolution of the Jeans mass and $M_{mgr}(t) \equiv \rho \cdot 2z \cdot \lambda_{mgr}^2$ is shown in Fig.10, where λ_{mgr} is the wave length for which the perturbation grows fastest. We estimate $\lambda_{mgr} \simeq 2\pi \cdot 2z$ (Larson 1985 [27]) in this paper. In Fig.10, the gravitational force and the pressure gradient force balance where the two lines approach to the nearest point with each other, and our calculation is stopped at this point. We estimate the mass of the fragments with the definition $M_{frag} \equiv M_{mgr}(t_f)$, where t_f is the time that the condition (3.17) is satisfied. We also calculated the mass of the fragments for a wide variety of initial conditions (Fig.11). It is obvious that spherical symmetry is a very special configuration

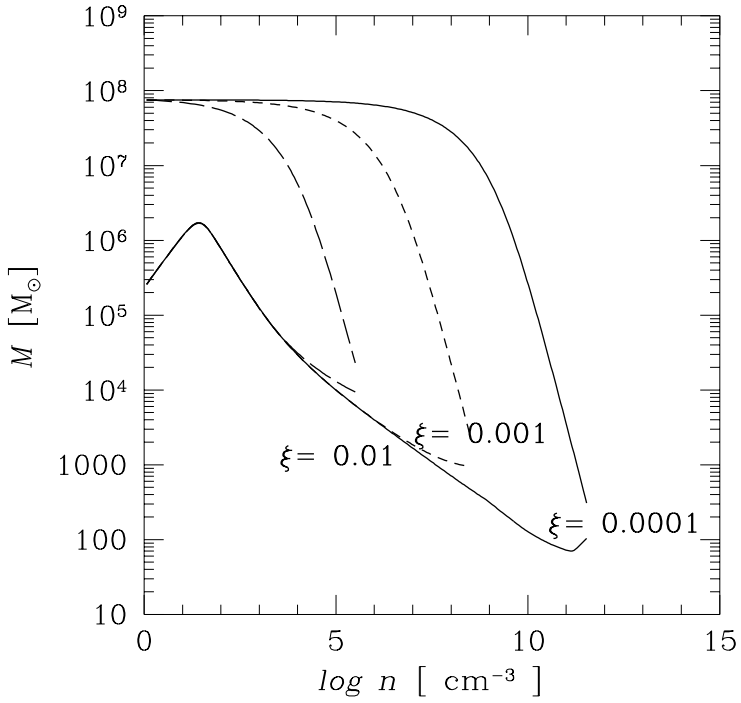

Figure 10: *The evolution of the Jeans mass and the mass of the fragmentation for the initially spherical rotator, in the $n - M$ plane. The mass of the fragments are estimated as $M_{frag} = 2\rho z \lambda_{mgr}^2$ (see text) .*

for the thermal evolution of a collapsing cloud. Three body reactions to produce hydrogen molecules are only effective when the initial shape is extremely spherical or the initial configuration is prolate, and has extremely low angular momentum.

In the region that the cloud is oblate ($\alpha_0 < 1$), the fragment mass has almost no dependence on ξ for small ξ. This can be understood naturally as follows: The deformation effect simply by the gravitational instability exceeds the effect by the angular momentum barrier for small ξ. In other words, the disk collapses to a very thin disk before the bounce due to the angular momentum occurs.

In case the cloud is prolate ($\alpha_0 > 1$), a cloud whose angular momentum vector is parallel to the major axis of the cloud finally forms a thin disk whose radial gravity is supported by the angular momentum barrier, as was mentioned in subsection 3.2. We can see that there is a "trough"on $\alpha_0 - \xi$ plane at $10^{-1.5} \lesssim \xi \lesssim 10^{-1}$, which corresponds to the value ξ_E, ξ_B described by the equation (41) in Hutchins (1976) [20]. The definition of ξ_E, ξ_B are as folows: if $\xi > \xi_B(\alpha_0)$, no bounce occurs by the angular momentum barrier and the collapse finishes. If $\xi > \xi_E(\alpha_0)$, the density does not decrease after the bounce until the collapse finishes.

The "trough" structure is understood as follows: if $\xi > \xi_E(\alpha_0)$, the collapse is almost the same as the disk collapse, therefore M_{frag} is larger than that in the case $\xi < \xi_E(\alpha_0)$.

If $\xi_E(\alpha_0) > \xi > \xi_B(\alpha_0)$, the density always increases, the surface density also increases

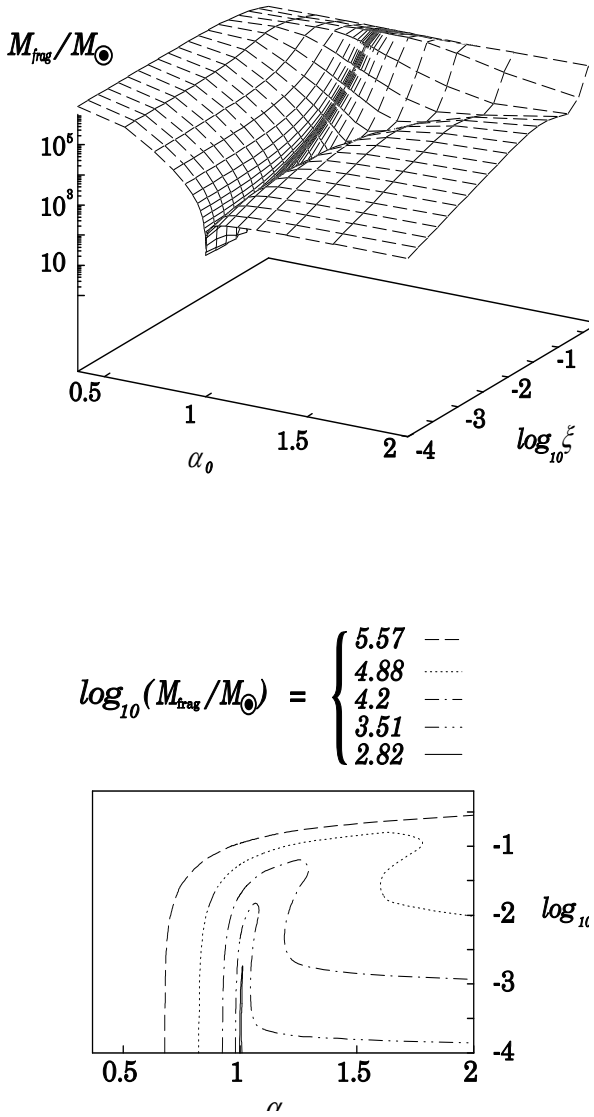

Figure 11: *The upper figure shows M_{frag} for various values of α_0, ξ. The lower figure shows the contour plot of M_{frag} on the $\alpha_0 - \xi$ pane in the upper panel.*

and M_{frag} decreases. It is different from the case of disk collapse. Finally, if $\xi < \xi_B(\alpha_0)$, due to the strong bounce in R direction, the density decreases and M_{frag} is larger than in the previous case. If ξ is small enough, H_2 is produced during the bounce, and the corresponding cooling proceeds. Then M_{frag} is smaller than that for $\xi \simeq \xi_B(\alpha_0)$.

3.7 Conclusions & discussion

We have shown the thermal evolution of the collapse of primordial gas clouds with non-spherical initial configuration and/or with some angular momentum. We found the frag-

ment mass is very sensitive to the initial configurations.

In the case of initially oblate clouds, they immediately collapse to form a thin disk, and the gravitational force balances with the pressure gradient force before H_2 dissociation. Hence the two characteristic Jeans mass scales at H_2 dissociation and H ionization mentioned by Carlberg (1981) [5] do not play important roles.

In the case of initially extremely spherically symmetric clouds, the evolution of these clouds are affected greatly by the value of the angular momentum. If the spin parameter ξ is much larger than some critical value 10^{-4} , the dissociation of the hydrogen molecules sets in before the three body reactions, which produce hydrogen molecules, becomes effective. If the spin parameter ξ is smaller than 10^{-4}, the three body reactions can be effective before the temperature rises so high that the hydrogen molecules dissociate.

In the case of initially prolate clouds, the angular momentum also plays an important role, but the three body reactions are not important for the realistic values of ξ, or for larger mass scale of the cloud. We also calculated the fragment mass M_{frag} for various α_0 and ξ. Then the mass is much above the ordinary stellar mass for realistic value of α_0 or ξ. In consequence, we must conclude that an initially spherical configuration is a very special and unrealistic one.

Our assumed configurations, in which the angular momentum vector is parallel to the axis of the symmetry of the cloud, are not realistic, because the tidal interaction between the density perturbations cannot induce the angular momentum parallel to the axis of symmetry. In case we treat the triaxial ellipsoids, it is easily understood that the angular momentum is not parallel to any axis in general. In such cases, the angular momentum could play an important role, because the disk like collapse is stopped by the angular momentum which is not parallel to the axis of symmetry.

In this paper, as mentioned in subsection 3.6, M_{frag} is defined as the Jeans mass at the time essentially (3.17) is satisfied, i.e., we stopped our calculation when the gravitational force balances with the pressure gradient force for the first time. In reality, the cloud does not stop dynamical evolution, and does not fragment at this time, since t_{dyn} is much smaller than t_{ff} (see equation (3.19)). After the cloud dissipate the kinetic energy, it settles into an equilibrium state for z-direction. According to Inutsuka & Miyama (1992) [21], when the condition

$$t_{dyn} \equiv \rho / \frac{d\rho}{dt} \gtrsim t_{mgr}, \tag{3. 23}$$

is satisfied, where

$$t_{mgr} \simeq (\frac{G\rho}{\Omega\pi})^{-1/2}, \tag{3. 24}$$

and if the cooling is effective, the cloud will fragment into smaller filaments. Here, t_{mgr} is the maximal growth rate of the density perturbation in the equilibrium sheet, where Ω is a non-dimensional constant ($\sim O(1)$), which almost equals 5 in case the sheet is isothermal (Larson 1985 [27]). In this phase, we can argue the true mass of the fragments. Since the cloud is highly flattened ($\alpha \ll 1$) in this phase, the radius shrinks little before vertical equilibrium is satisfied, and the surface density changes little, too. Thus, the true fragment

mass scale is determined by the temperature, T_{fr}, at the time t_{fr}, when equation (3.23) is satisfied. In the course of dissipating the kinetic energy, the cloud would be shock heated, because the collapse of the cloud is supersonic, and keep cooling during the entire time. T_{fr} and the fragment mass scales are increased by the shock heating, and decreased by the cooling.

It is necessary to investigate the process from t_f to t_{fr}, in order to estimate the accurate fragment mass scales. However, they may not be much different from M_{frag}. Since the shock velocity, v_s is not too high ($v_s \lesssim 10$km/s) with the parameters of this paper, T_{fr} must be lower than 10^4K, and $T_{fr} \gtrsim 10^3$K because the cooling rate of H_2 is very low for $T < 10^3$K. If $v_s \gtrsim 50$km/s, the shock heating would cause a more complicated situation, with the ionization of hydrogen atoms (SK [50]). In the course of dynamical cooling process, the over abundance of electrons is caused due to the slow recombination rate compared to the atomic cooling rate. What is more, those electrons can be the catalyst for the H_2 production. As a consequence, serious amount of molecular cooling is expected below 10^4K in this dynamical situation (SK [50]). Then, qualitatively different results may be expected. If we wish to treat this problem properly, we need an one dimensional hydrodynamical calculation.

In the second place, the cloud would fragment into filaments rather than the blobs according to the nature of gravity. Then, the filaments would collapse and bounce to form an equilibrium states. In this phase, the fragmentation will set in again. Further discussion will be coming up in later sections.

4 Fragmentation of cylinder

Following the scenario presented in the previous section, we investigate the dynamical and thermal evolution of infinitely long cylinders to model filaments formed in the post shock cooled sheet and estimate the minimum mass of the fragments of the cylinders. Uehara et.al. (1996) [60] have found that the minimum mass is essentially determined by the *Chandrasekhar mass*.

4.1 Basic equations

4.1.1 Equation of motion of the cloud for cylindrical collapse

For an isothermal cylinder there is a critical line density $M_c(T)$ (Ostriker 1964)[39]given by

$$M_c(T) = \frac{2kT}{\mu m_{\rm H} G}, \tag{4.1}$$

where T, μ, and $m_{\rm H}$ represent the isothermal temperature, the mean molecular weight and the mass of hydrogen atoms, respectively. An isothermal cylinder with line density M larger than $M_c(T)$ has no equilibrium and collapses, while an isothermal cylinder with M less than $M_c(T)$ expands if the external pressure does not exist. This is quite a specific feature of cylinders, since sheets and spherical clouds can achieve equilibria for any temperature by the modification of their densities.

When the cylindrical cloud is formed as a result of the fragmentation of the sheet, the gas pressure is comparable to the gravitational force. Therefore, the effect of the gas pressure must be included in the equation of motion of the cylindrical cloud. To know the dynamical evolution of such a cylinder we begin with the virial equation for a cylinder,

$$\frac{1}{2}\frac{d^2 I}{dt^2} = 2T + 2\Pi - GM^2, \tag{4. 2}$$

where

$$I = \int_V \rho r^2 dV, \quad T = \int_V \frac{1}{2}\rho u^2 dV, \quad \Pi = \int_V p dV, \tag{4. 3}$$

and the integration is effected over the volume per unit length of the cylinder, V. Here we approximate that the cylinder is uniform and has constant density ρ, scale radius $R = \sqrt{M/\pi\rho}$, and temperature T. Then above I, T, and Π become

$$I = \frac{1}{2}MR^2, \quad T = \frac{1}{4}M\left(\frac{dR}{dt}\right)^2, \quad \Pi = \frac{kT}{\mu m_{\rm H}}M \ . \tag{4. 4}$$

Substituting (4. 4) in equation (4. 2) we obtain

$$\frac{d^2 R}{dt^2} \ = \ -\frac{2G}{R}(M - M_c(T)) \ . \tag{4. 5}$$

We describe the evolution of the cylinder by this equation.

4.1.2 Energy equation and chemical reactions

The equations describing thermal processes are the same as those of section 3. The time evolution of the cloud temperature is described by the energy equation given by

$$\frac{d\epsilon}{dt} = -P(T,\rho)\frac{d}{dt}\frac{1}{\rho} - \Lambda(T,\rho) \ , \tag{4.6}$$

where ϵ, and Λ are the thermal energy per unit mass , the cooling/heating by radiation and chemical reactions, respectively. In Λ we take into account H_2 line emissions due to the vibrational and rotational transitions between excited levels. The gas pressure P is evaluated by the equation of state of the ideal gas. The details of Λ are shown in section 2, Appendix A and Appendix B.

We use the same chemical reaction rates as Palla et al. (1983) [40]. We consider H, H_2, H^+, H^-, and e^- as chemical compositions of the cloud. Helium and its ions are not included in our calculations because they are chemically inert at such low temperatures ($T \lesssim 10^4$K) as considered here. Hereafter we use f_i to denote the fractional number abundance of the i-th composition.

4.2 The epoch of fragmentation and the mass of a fragment

The dispersion relation of the linear density perturbations of an isothermal sheet with surface density Σ shows that the perturbation with wavelength $\lambda_{frag} \sim 4\pi H$ grows fastest, where $H = c_s^2/\pi G\Sigma$ and $c_s = \sqrt{kT/\mu m_{\rm H}}$ is the sound velocity (Simon 1965)[53]. Although the primordial gas clouds we consider are not isothermal, the dispersion relations are weakly dependent on equation of state (see Fig.1 of Larson 1985)[27] and we use the isothermal dispersion relations as typical ones. As shown by Miyama et al. ([35], [36]), an equilibrium sheet tends to fragment into filaments, whose line density is estimated by

$$M = \lambda_{frag}\Sigma \sim \frac{4kT}{\mu m_{\rm H} G}. \tag{4. 7}$$

Since the above M is greater than $M_c(T)$ the filament formed by fragmentation of an isothermal sheet cannot be in an equilibrium configuration but begins to collapse. As shown by Inutsuka & Miyama (1992) [21] such a cylinder with $M > M_c(T)$ does not fragment immediately. To estimate the epoch of the fragmentation of a collapsing cloud we should compare the dynamical time scale of collapse defined by $t_{dyn} = \rho/\frac{d\rho}{dt}$ with that of fragmentation, t_{frag}. When $t_{dyn} \lesssim t_{frag}$, the cylinder collapses so fast that the density perturbation does not grow similar to the spherical case. The collapsing cloud fragments when the condition

$$t_{dyn} \sim t_{frag}, \tag{4.8}$$

is satisfied, i.e. when the collapse almost stops. In such a situation we can apply the perturbation analysis of the equilibrium sheet and the cylinder.

In the case of the isothermal cylinder in equilibrium, the perturbation with wavelength $\lambda_{frag} \sim 2\pi R$ grows fastest, where R is the scale radius of the cylinder defined by $R = \sqrt{M/\pi\rho_0}$ with M and ρ_0 being the line density and the central density, respectively. The

e-folding time scale of the fragmentation is given by $t_{frag} = 2.1/\sqrt{2\pi G\rho_0}$, (Nagasawa 1987) [37]. The mass of the fragment formed by the fragmentation of the isothermal cylinder is estimated by

$$M_{frag} = \lambda_{frag} M \sim 2\pi R M. \tag{4. 9}$$

In our model we estimate the mass of the fragment by equation (4. 9) at the epoch when the condition (4. 8) is satisfied.

4.3 The results of numerical calculations

To obtain initial conditions of a cylindrical cloud which is formed by the fragmentation of the post shock cooled sheet, we recalculate a typical case of SK with $z = 5, \Omega_b h^2 = 0.1$, and shock velocity $v_s = 200\mathrm{km\,s^{-1}}$. As initial conditions of our cylindrical cloud we adopt physical parameters of the post shock one dimensional flow at the point when the cooling time of the sheet ($\sim$ the dynamical time scale of the sheet) becomes equal to the time scale of the fragmentation, so that the sheet is expected to fragment into filaments. The initial condition of the cylinder thus obtained is $n_0 = 6.9\mathrm{cm^{-3}}, T_0 = 330\mathrm{K}$, $f_{\mathrm{H_2},0} = 2.3 \times 10^{-3}$, and $f_{\mathrm{e^-},0} = 2.7 \times 10^{-4}$. Under the above initial condition we calculated for the cases $M/M_c(T_0) = 1.0,\ 1.3,\ 1.5,\ 1.7$, and 2.0 (case A$\sim$E, see Table 5), for comparison.

Since the equilibrium sheet tends to fragment into the cylinder of line density $M \sim 2M_c(T_0)$ (eq. [4. 1, 4. 7]), we show the evolution for case E as representative, for which the mass of the fragment becomes minimum. The evolution on the n-T (number density - temperature) plane and virial temperature (eq. [4. 11]) are shown in Figure 12a. From Figure 12a we can see that the cylinder continues to collapse even after the cloud becomes optically thick to the line emission of hydrogen molecules ($n \gtrsim 10^{10}\mathrm{cm^{-3}}$). The fact that the cloud can collapse isothermally as a function of time by radiative cooling ($n \gtrsim 10^{12}\mathrm{cm^{-3}}$) is the characteristic feature of the cylindrical shape of the cloud, for which the gravitational force is proportional to R^{-1}. Since temperature becomes constant, hydrogen molecules does not dissociate. Figure 12b shows two time scales t_{frag} and t_{dyn} normalized by the initial free-fall time scale ($1/\sqrt{2\pi G\rho_0}$) and the mass of the fragment (eq. [4. 9]). Comparing two time scales, we conclude that the collapsing cylinder fragments at $n \sim 3 \times 10^{12}\mathrm{cm^{-3}}$ and the mass of the fragment becomes $\sim 2M_\odot$ for case E.

In Table 5 number density n, hydrogen molecule fraction $f_{\mathrm{H_2}}$ when the fragmentation occurs (column 3 and 4, respectively), and the mass of the fragment M_{frag} (column 5) are listed for each line densities M (column 2). ¿From Table 5 we can see the tendency that the larger the initial line density M, the smaller the mass of the fragment M_{frag} and M_{frag} converges to several solar mass for larger line densities. Interpretation of these results will be stated in the next section.

4.4 Analytical estimate of the minimum fragment mass

It is interesting to ask what determines the mass of the fragments of the collapsing cylinder for case E. The collapsing cylinder fragments when the condition (4. 8) is satisfied. As the cylinder collapses isothermally as a function of time finally, we can set $d\epsilon/dt \sim 0$ in equation (4. 6) and from this we obtain $t_{dyn} \sim (\gamma - 1)\, t_{cool}$, where $\gamma = 7/5$ for diatomic

molecular gas. Since the cloud cools by the line emissions of hydrogen molecules and is optically thick to these lines emission, t_{cool} can be estimated by

$$t_{cool} \sim \frac{\frac{1}{\gamma-1}\frac{M}{\mu m_{\rm H}}kT}{2\pi R\sigma T^4 \frac{\Delta\nu}{\nu}\alpha_c}, \tag{4.10}$$

where $\sigma = 2\pi^5 k^4/15h^3c^2$ is the Stefan-Boltzmann constant, and α_c is the effective number of line emissions. Since the optical depth is ~ 100 at most, the wing of line profile may not be important (Rybicki & Lightman 1987) [49] and the line broadening is determined by Doppler broadening as $\Delta\nu/\nu = v_{\rm H_2}/c = \sqrt{kT/m_{\rm H}c^2}$. The effects of chemical heating/cooling are not included in t_{cool} because the fraction of hydrogen molecule $f_{\rm H_2}$ is almost unity by the epoch of the fragmentation. The temperature of the cylinder is estimated by the virial temperature as

$$kT = \frac{1}{2}\mu m_{\rm H} GM. \tag{4.11}$$

From the above equations we obtain

$$M_{frag} \sim 2\pi RM \sim \sqrt{\frac{1}{\alpha_c}}\frac{1}{\mu^{9/4}}\frac{m_{Pl}^3}{m_{\rm H}^2}, \tag{4. 12}$$

where $m_{Pl} = \sqrt{hc/G}$ is the Planck mass. Equation (4. 12) means that M_{frag} is essentially equal to the Chandrasekhar mass ($\sim m_{Pl}^3/m_p^2$, here m_p is proton mass).

So far we did not consider other heating processes such as shocks and turbulence which likely to occur in the collapsing cloud. All these processes tend to halt the collapse, so that the epoch of fragmentation becomes earlier and, as a result, the mass of fragment increases. So equation (4. 12) gives the lower limit on the mass of the fragment which is formed from the primordial gas cloud. Our estimate shows even the primordial gas cloud which cools most effectively by hydrogen molecules cannot fragment into a smaller mass than equation (4. 12).

For smaller line densities the gas pressure force halts the collapse before three-body reactions (Palla et al. 1983)[40] *completely* convert atomic hydrogens to molecules. In these cases equation (4. 12) is not applicable because clouds are optically thin to line emissions for $f_{\rm H_2} \lesssim 10^{-1}$ and chemical heating by $\rm H_2$ formation must be considered when hydrogen molecules are formed by three-body reactions. These clouds fragment at lower density, in other words at larger scale radius, than the density at which they reach the isothermally collapsing stage (corresponding to $n \gtrsim 10^{12}{\rm cm}^{-3}$ of case E). Since M_{frag} is proportional to the scale radius at fragmentation, this leads to the larger fragment mass.

4.5 Discussions

The opacity-limited hierarchical fragmentation scenario was argued by several authors (Low & Lynden-Bell 1976[30]; Rees 1976 [46]; Silk 1977 [52]). According to Rees (1976)[46],

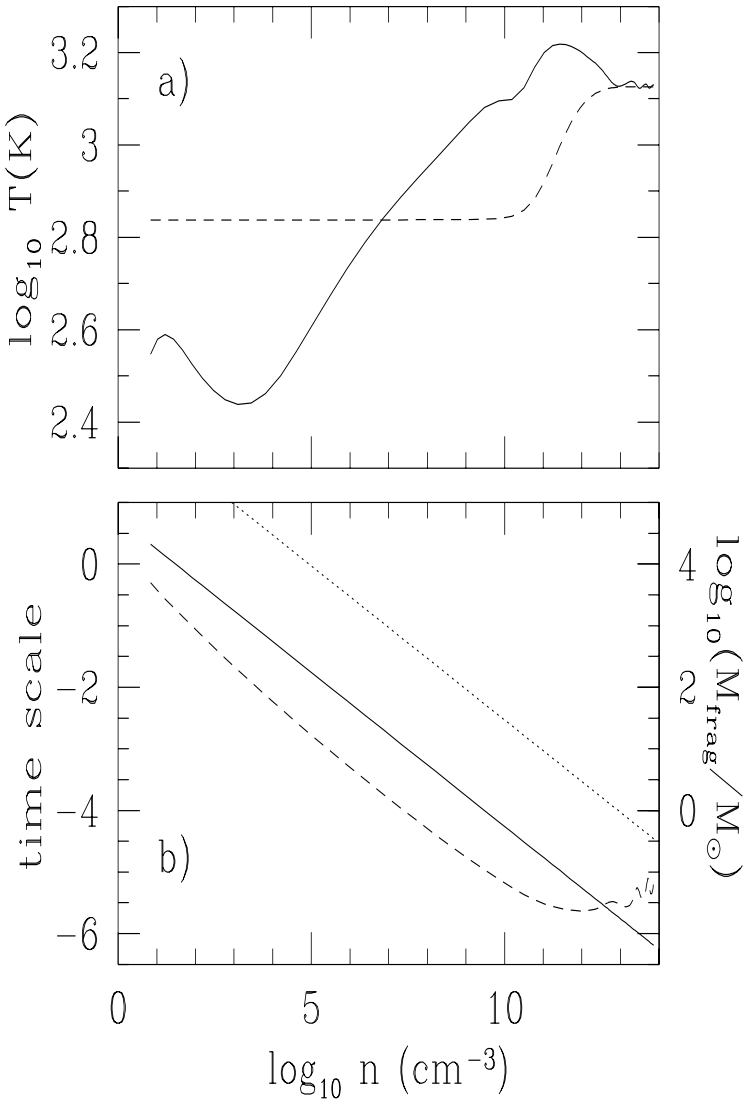

Figure 12: a) The thermal evolution of a cylindrical cloud on the n-T plane (solid curve) for case E. The virial temperature is also plotted(dashed curve). b) Evolution of time scales and mass of a fragment for case E. Time scales are normalized by the initial free-fall time. At first the time scale for collapse, t_{dyn}(dashed curve), is shorter than that for fragmentation, t_{frag}(solid curve), by an order of magnitude. But finally t_{frag} becomes shorter than t_{dyn}, at which the collapsing cylinder is thought to fragment and the mass of a fragment(dotted curve) becomes $\sim 2M_\odot$.

Table 5: Initial Line Density and Results of Numerical Calculations

Case	$M/M_c(T_0)$	$n(\mathrm{cm}^{-3})$	f_{H_2}	$M_{frag}/M_\odot$
A	1.0	1×10^{8}	5×10^{-3}	1×10^{2}
B	1.3	1×10^{9}	4×10^{-2}	4×10^{1}
C	1.5	2×10^{10}	4×10^{-1}	2×10^{1}
D	1.7	5×10^{11}	9×10^{-1}	3×10^{0}
E	2.0	3×10^{12}	1×10^{0}	2×10^{0}

the minimum Jeans mass of the spherical cloud is given by

$$M_F = \left(\frac{kT}{m_{\mathrm{H}}c^2}\right)^{1/4} f^{-1/2}\frac{1}{\mu^{9/4}}\frac{m_{Pl}^3}{m_{\mathrm{H}}^2},$$

where f ($\lesssim 1$) is the efficiency of the radiation of the cloud compared with the black body radiation and it depends on the details of the cooling process and the opacity. As the present molecular clouds have various molecules and grains, f is nearly equal to unity when the cloud becomes optically thick to the radiation. In the case of the primordial gas cloud which is cooled by line emissions of hydrogen molecules, f is proportional to $\sqrt{T}$ (Doppler broadening) and T-dependence of M_F completely vanishes. Apparently this gives the same conclusion as ours. However previous authors argued the spherical collapse, which does not lead to fragmentation, and our argument would be more relevant.

Although our analysis cannot estimate the exact mass of the fragment, the existence of the lower limit on the mass of the fragment we found would have significant meanings. For example, the following scenario for formation of our Galaxy may be possible: the existence of lower limit on the fragment mass cause the mass of the first stars to be massive, so that the first stars complete main-sequence stage within the age of the universe and evolve to dark remnants (e.g. white dwarfs, neutron stars, and black holes) in the Galactic halo after some mass loss, whose gas fall to the Galactic disk to form it. This scenario would be consistent with infall model (Lynden-Bell 1975[31]; Vader & de Jong 1981[63]; Clayton 1988[8]), which was proposed to explain G dwarf problem (the observed paucity of metal-poor stars, see Rocha-Pinto & Maciel 1996 [48] for recent observation). Remnants thus formed by the above scenario may be MACHOs, whose estimated mass ($\sim 0.5M_\odot$, Bennett et al. 1996 [2]) is consistent with that of white dwarfs. It is very interesting that some of astrophysical problems, including non-existence of zero metal stars, may be explained in a consistent way by such a simple scenario.

5 Thermal evolution behind the shock in primordial gas : A semi-analytic approach

In this section a semi-analytic investigation of the thermal evolution in the postshock region in the primordial gas cloud is presented. As was mentioned in section 1, the evolution of post shock region in the primordial gas cloud is highly dynamical, because the cooling time is not always faster than the time scales of many reactions. However, comparing the important time scales, we find that the evolutionary path of the post shock region is predictable without any dynamical calculation.

5.1 The time scales

In this subsection we compare the time scales which is essential to the thermal evolution of the post shock layer in the primordial gas cloud. First of all, we enumerate the definition of the time scales,

$$t_{cool} \equiv \frac{\gamma}{\gamma-1}\frac{\rho kT}{\mu m_p \Lambda}, \tag{5. 1}$$

$$t_{ion} \equiv \frac{n_H}{k^{ion} n_H n_e} = \frac{1}{k^{ion} n_N y_e}, \tag{5. 2}$$

$$t_{rec} \equiv \frac{n_e}{k^{rec} n_e n_p} = \frac{1}{k^{rec} n_N y_e}, \tag{5. 3}$$

$$t_{dis} \equiv \frac{n_{H_2}}{\sum_i k_i^{dis}\, n_{H_2} n_i} = \frac{1}{\sum_i k_i^{dis}\, n_N y_i}, \tag{5. 4}$$

$$t_{for} \equiv \frac{n_{H_2}}{\sum_{ij} k_{ij}^{for}\, n_i n_j} = \frac{y_{H_2}}{\sum_{ij} k_{ij}^{for}\, n_N y_i y_j}, \tag{5. 5}$$

where $t_{cool}, t_{ion}, t_{rec}, t_{dis}$ and t_{for} denote the time scale of cooling, ionization, recombination, H_2 dissociation and formation, respectively. n_N, n_i, y_i, k^X, ρ, μ and m_p are the number density of nucleons, the number density of the ith species, the fraction of ith species defined as $y_i \equiv n_i/n_N$, the reactional rate coefficient of the "X" process, density, mean molecular weight and proton mass. Comparing these five time scales we can find the fastest process without detailed dynamical calculations.

We should remark that *all of those time scales are proportional to* ρ^{-1}, because every process is collisional. The dominant component of the cooling is changing according to the temperature of the cloud. Below 10^4K, H_2 line emission dominates the total cooling rate of the cloud. In this process, the cooling rate is proportional to the number density of the H_2 at the excited levels whose fraction is proportional to ρ^2 (section 2) [4]. Hence, the time scale is proportional to ρ^{-1} as in equation (5.1). The cooling process in $10^4\mathrm{K} \lesssim T \lesssim 10^5\mathrm{K}$ is dominated by the bound-bound transition of the hydrogen atoms, and the number of the excited hydrogen atom is determined by the collision with another atom. Therefore, the cooling rate is proportional to the square of the total density. For higher temperature ($T \gtrsim 10^5$K), the free-free emission by the collision between ions and electrons dominates

[4]This treatment is limited for low density ($n \lesssim 10^4\mathrm{cm}^{-3}$). The cooling rate is not proportional to ρ^2 for higher density (higher than the *critical density*).

the energy radiated away from the cloud. In any case, the cooling rate is proportional to ρ^2, and the cooling time is proportional to ρ^{-1} [5]. As a result, the ratio of any two time scales is independent of the total density. In the following subsections, we compare the time scales individually.

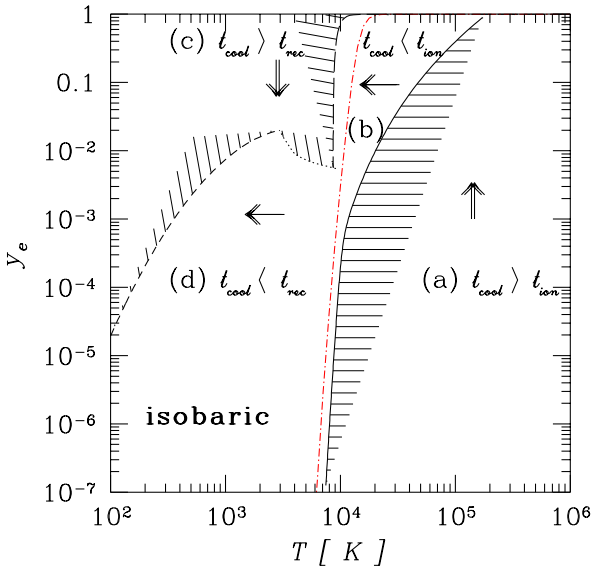

Figure 13: *The $y_e - T$ plane is divided into several regions in which the ratio of the time scales are different from each other. The arrows on the plane denote the direction of the thermal evolution of the post shock layer. The region (a) in which the condition $t_{cool} < t_{ion}$ holds is bounded by the solid line. In this region, ionization proceeds faster than the cooling, then the system evolves upward on the $y_e - T$ plane. On the other hand, in the region (b) and (d), the conditions $t_{cool} < t_{ion}$ and $t_{cool} < t_{rec}$ always holds. Therefore the temperature drops down before the system ionizes or recombines. The dot-short dashed line denote the line on which the equation $t_{rec} = t_{ion}$ holds. In the region (c), recombiantion proceeds faster than the cooling. The region (c) is bounded by the dotted line, short dashed line and the the long dashed line. Those three lines denote the lines on which the condition $\tau_{cool} = \tau_{rec}$ holds. The long dashed line is calculated by assuming that the cooling rate is dominated by the hydrogen line cooling. The dotted line is calculated assuming the chemical equilibrium of the hydrogen molecules, and the short dashed line is calculated with $f_{H_2} = 10^{-3}$, which is the frozen value of the hydrogen molecules for the shock velocity higher than ~ 30km/s, see also Fig.15.*

[5]The Compton cooling is effective at high redshift and high temperature. In this case, the cooling rate is not proportional to ρ^2 but it does not change the following results significantly.

5.1.1 Ionization and cooling

In this subsection, we compare the time scales of ionization and cooling. As was mentioned previously, the ratio t_{ion}/t_{cool} depends not on ρ, but on the ionization degree y_e and temperature T, because both of the processes are collisional. Hence the ratio t_{ion}/t_{cool} is determined at a point on the $y_e - T$ plane independently of the magnitude of density. The line along which t_{ion}/t_{cool} is equal to unity is shown in Fig.13. If the initial condition is given below the line, the system is ionized before it cools down, because $t_{ion}/t_{cool} < 1$. Otherwise, it is cooled before it ionizes. The expected evolutionary path is also expressed by the arrows in Fig.13.

5.1.2 Recombination and cooling

Here we examine the balance between the recombination process and the cooling process. The recombination process is important for $\lesssim 10^4$K . For $T \lesssim 10^4$K, the cooling process is not dominated by the atomic hydrogen line cooling but by the line cooling of the hydrogen molecules. Therefore the ratio t_{rec}/t_{cool} depends not only on the ionization degree and the temperature but also the fraction of hydrogen molecules. In order to draw the line $t_{rec}/t_{cool} = 1$ on the $y_e - T$ plane, we need the information on the fraction of hydrogen molecules. As will be discussed in the next subsection, the fraction of H_2 is determined by the reactional equilibrium above $\sim 10^4$K. Then it is frozen to a value below 5×10^3K. The line along which $t_{rec}/t_{cool} = 1$ is satisfied is drawn in Fig.13. In the region above the line, the system recombine before it cools down, and below the line, the system cools down before the recombination proceeds. The expected evolutionary path is also drawn in Fig.13 by the arrows.

5.1.3 The fraction of H_2

In this subsection, we check whether H_2 is in reactional equilibrium, or not. The fraction of hydrogen molecules is roughly determined by t_{dis} and t_{for}, which denote the time scale of the dissociation and the formation of hydrogen molecules. If both of the time scales are very short compared to the time scales, t_{cool} and t_{rec}, the fraction of the hydrogen molecules is given by the condition of reactional equilibrium with given value of y_e and T. Hence, the ratio $t_{dis}/t_{cool,rec}$ and $t_{for}/t_{cool,rec}$ should be examined.

First of all, we remark important properties of t_{dis} and t_{for}. The time scale of dissociation is independent of y_{H_2}, the fraction of hydrogen molecules. On the other hand, t_{for} is proportional to y_{H_2}. Then both of the time scales given in terms of their equilibrium values are,

$$t_{dis} = t^{eq}_{dis}, \tag{5. 6}$$

$$t_{for} = t^{eq}_{for} \frac{y_{H_2}}{y^{eq}_{H_2}}, \tag{5. 7}$$

where the suffix eq denotes the value at which the hydrogen molecules are in chemical equilibrium.

If the interesting time scale (t_{int}) which is to be compared with t_{dis} and t_{for} is independent of y_{H_2}, we have a general argument as follows: 1) In case $y_{H_2} > y^{eq}_{H_2}$, dissociation

proceeds faster than the formation process. Hence, t_{dis} controls the change of $y_{\rm H_2}$, that is why we do not have to concern about t_{for}. On the other hand t_{dis} is independent of $y_{\rm H_2}$, then $y_{\rm H_2}$ converge to $y_{\rm H_2}^{eq}$ if $t_{dis} < t_{int}$ is satisfied. 2) If $y_{\rm H_2} < y_{\rm H_2}^{eq}$, $y_{\rm H_2}$ is controlled by the time scale t_{for}, because the system will try to recover the fraction of H_2 which is smaller than the equilibrium value. The maximal value of t_{for} is the one at equilibrium since t_{for} is proportional to $y_{\rm H_2}$(eq.(5.7)). Therefore, if $t_{int} > t_{for}^{eq} (= t_{dis})$, t_{int} is always greater than t_{for}. As a result, $t_{int} > t_{dis}$ is the sufficient condition for the system to maintain the chemical equilibrium of hydrogen molecules.

Now first, let us check the reactional equilibrium of hydrogen molecules compared to the recombination process. In other words, we are going to check the magnitude of t_{dis}/t_{rec} and t_{for}/t_{rec}. As was discussed previously, when we compare t_{dis} and t_{for} with the other time scales which do not depend on $y_{\rm H_2}$, we do not have to concern about t_{for}. In this case, t_{rec} is independent of $y_{\rm H_2}$, hence we only have to examine t_{dis}/t_{rec}. The time scale of recombination, t_{rec} (5.3) is proportional to y_e^{-1}, and the time scale of dissociation is also proportional to y_e^{-1}, because it is governed by the collision between H^+ and H_2. This means that the ratio t_{dis}/t_{rec} is independent of y_e. It does also not depend on $y_{\rm H_2}$, hence the ratio just depends on the temperature. Therefore we have the critical temperature above which t_{dis}/t_{rec} is greater than unity. This critical temperature is ~ 2300K. This argument is different if the ionization degree is sufficiently low enough for the $H - H_2$ collision to dominate the $H^+ - H_2$ collision. However, within the region we are interested ($y_e \gtrsim 10^{-5} - 10^{-6}$), ionization degree is high enough. Therefore this treatment is valid.

Next, let us check the reactional equilibrium of H_2 with respect to the cooling of the gas, i.e. check the ratio t_{dis}/t_{cool} and t_{for}/t_{cool}. However we cannot use the previous argument in this case because the cooling time scale depends on $y_{\rm H_2}$ for $T \lesssim 10^4$K. Accordingly, we need to investigate the individual case again. 1) If $y_{\rm H_2} < y_{\rm H_2}^{eq}$, we get the relation $t_{for} < t_{dis}$. In this case, we do not have to pay attention to t_{dis} because H_2 has smaller fraction than its equilibrium value. The ratio t_{for}/t_{cool} is almost proportional to $y_{\rm H_2}^2$, because t_{for} is proportional to $y_{\rm H_2}$ and t_{cool} is proportional to $y_{\rm H_2}^{-1}$. Therefore the ratio reaches a maximal value at $y_{\rm H_2} = y_{\rm H_2}^{eq}$. This means t_{for}/t_{cool} is always smaller than $t_{for}^{eq}/t_{cool}^{eq}$. Then, if $t_{for}^{eq}/t_{cool}^{eq}$ is smaller than unity, H_2 is in equilibrium with respect to the cooling process. 2) If $y_{\rm H_2} > y_{\rm H_2}^{eq}$, we get $t_{for} > t_{dis}$. In this case we just check the ratio t_{dis}/t_{cool} because H_2 has larger fraction than its equilibrium value. The ratio t_{dis}/t_{cool} is proportional to $y_{\rm H_2}$. Therefore, the ratio does not reach a maximum at $y_{\rm H_2} = y_{\rm H_2}^{eq}$, but a minimum. Then we cannot decide that $t_{dis}^{eq}/t_{cool}^{eq} < 1$ is the sufficient condition for the reactional equilibrium according to the cooling process. However, in the region $y_{\rm H_2} > y_{\rm H_2}^{eq}$, the fraction of H_2 converges to $y_{\rm H_2}^{eq}$ because the *inclination of the line*, $t_{dis}/t_{cool}^{eq} = 1$ *is negative in Fig.*15. In other words, if the hydrogen molecules are not in reactional equilibrium in $y_{\rm H_2} > y_{\rm H_2}^{eq}$, the cooling process proceeds faster than dissociation process, however, after the system cools down to the line $t_{dis}/t_{cool}^{eq} = 1$ the fraction of hydrogen molecules converge to the equilibrium value. Anyway, if the condition $t_{dis}/t_{cool}^{eq} < 1$ is satisfied, the relation $y_{\rm H_2} \simeq y_{\rm H_2}^{eq}$ always holds.

5.2 Comparison with the numerical calculation

In this subsection we compare the results obtained in the previous subsection with numerical calculations. The numerical calculations which we performed are the same as the one in SK, except on one point that our calculations do not contain heliums (Appendix C and Appendix D) .

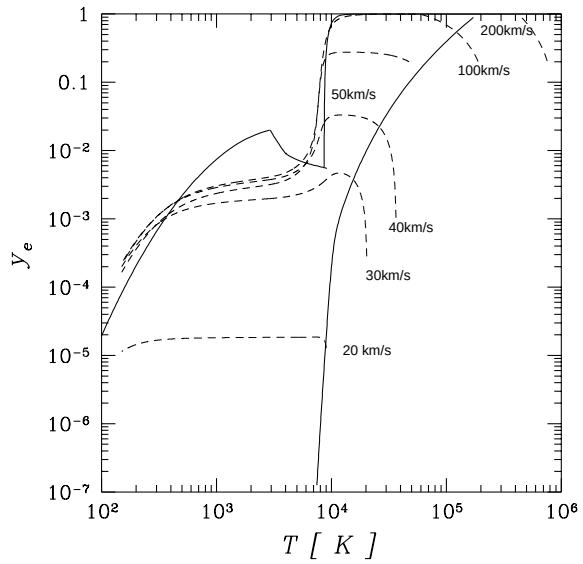

Figure 14: *The evolution of post shock layer in $y_e - T$ plane is presented. The solid lines are the boundaries beyond which the direction of the evolution is changed, and each line has the same meaning as in Fig.*13*. The short dashed lines are the numerical results in SK-type calculation. Each suffix denotes the initial shock velocity.*

Fig.14 shows the evolution of y_e to the temperature behind the shock front in the steady flow. It is obvious that the expected evolutionary path in Fig.13 coincides with the numerically calculated path. We also find that there exists a critical value of the initial shock velocity beyond which the evolution of y_e converges below 10^4K. The critical value of shock velocity is ~ 30km/s. The convergence of the ionization degree is essentially due to the reactional equilibrium of hydrogen molecules. The evolution of y_{H_2} is presented in Fig.15. The reactional equilibrium for hydrogen molecule holds outside of the shaded region on the $y_e - T$ plane. Once the system comes into the shaded region, the fraction of H_2 is frozen to a value, because the cooling time becomes faster than the dissociation and formation of hydrogen molecules. The frozen value of f_{H_2} is 10^{-3} for $v_s \gtrsim 30$km/s, and smaller for slower shock velocity. The frozen value degenerates for faster shock velocity, because the ionization degree also degenerates for $v_s \gtrsim 30$km/s.

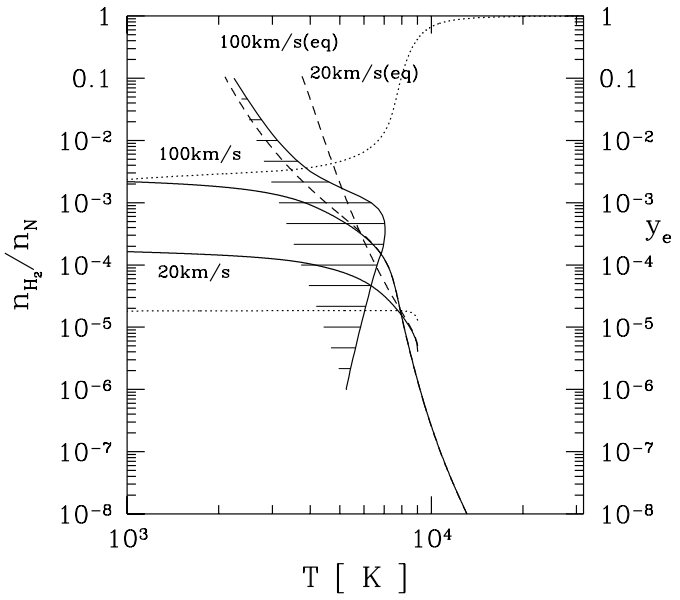

Figure 15: *The equilibrium and non-equilibrium fraction of hydrogen molecules are drawn in* $n_{\rm H_2}/n_H - T$ *plane. The solid lines labeled as* 100km/s *and* 20km/s *denote the dynamically calculated evolutionary path of the fraction of hydrogen molecules. The short dashed lines denote the fraction calculated from the chemical equilibrium of hydrogen molecules with dynamically calculated ionization degree which is denoted by the dotted lines. The boundary of the shaded region in* $y_e - T$ *plane is determined by the equation* $t_{cool} = t_{diss}$*. In the shaded region in* $y_e - T$ *plane, the chemical equilibrium of hydrogen molecules breaks down, and the fraction* $n_{\rm H_2}/n_H$ *freeze. The dotted lines labeled as* 100km/s *and* 20km/s *denote the evolutionary path of* y_e*.*

5.3 Conclusion

In this section, we investigate the thermal evolution of post shock layer in primordial gas clouds. Because of the delay of the recombination process compared to *the line cooling due to the hydrogen molecules*, significant amounts of electrons ($y_e \sim 10^{-3}$) remain below 10^4K. Feeded the electrons, H_2 also keeps high abundance ($y_{\rm H_2} \sim 10^{-3}$) for $10^3{\rm K} \lesssim T \lesssim 10^4{\rm K}$, then the cloud temperature drops to $T \sim 100$K quickly due to the H_2 line cooling. We have shown that both of the residual value of y_e and $y_{\rm H_2}$ are universal for $v_s \gtrsim 30$km/s by using semi-analytic treatment. These results for steady flow help us to understand the behavior of the dynamical evolution presented in later sections.

6 1- dimensional hydrodynamical approach

The knowledges obtained in the one-zone models in section 3 and section 4 presents a rough estimate of the mass of the fragments in the primordial gas clouds. However, those models seem to be too simple, especially for the first fragmentation from the disk to cylinders, because the strong shock is expected during the disk collapse. Following this point of view, the detailed calculations for the thermal evolution of the post shock layers in the primordial gas clouds are presented in section 5, but the argument is restricted for the steady shock, unfortunately. In fact, the shock in the gravitationally collapsing disk is not steady, and the complicated structures and highly dynamical situations are expected. In this section, which is the main part of this paper, the 1-D hydrodynamical calculation with detailed chemical reactions and radiative coolings are presented. Many interesting phenomenon are found in the collapsing cloud. We also argue the mass of the fragment at the end of this section.

6.1 Basic equations

In this subsection, we list the basic equations of our hydrodynamical calculation. First, the ordinary hydrodynamical equations are listed below.

$$\frac{\partial \tau}{\partial t} - \frac{\partial u}{\partial m} = 0, \tag{6. 1}$$

$$\frac{\partial u}{\partial t} + \frac{\partial p}{\partial m} = g, \tag{6. 2}$$

$$\frac{\partial E}{\partial t} + \frac{\partial (up)}{\partial m} = ug - \Lambda(\rho, T, y_i), \tag{6. 3}$$

where,

$$\tau \equiv \frac{1}{\rho}, \tag{6. 4}$$

$$E = \frac{p}{\rho(\gamma - 1)} + \frac{u^2}{2}, \tag{6. 5}$$

$$m(z) \equiv \int_0^z \rho(z) dz, \tag{6. 6}$$

$$g \equiv 2\pi G m(z). \tag{6. 7}$$

Here, $\rho, E, p, u, z, m(z), G, g$ and $\Lambda(\rho, T, y_i)$ denote the density, the total energy per unit mass, the thermal pressure, the expanding velocity in the vertical direction, the length measured from the center of the cloud in the vertical axis, the colum density, the gravitational constant, the gravitational force and the net energy loss per unit mass due to the radiative and chemical cooling (section 2), respectively. The time derivative $\partial/\partial t$ denotes the Lagrange derivative. We also solve the following chemical reactions.

$$\frac{dy_i}{dt} = \sum_j k_j y_j + n_{\rm H} \sum_{k,l} k_{kl} y_k y_l + n_{\rm H}^2 \sum_{m,n,s} k_{mns} y_m y_n y_s, \tag{6. 8}$$

where y_i and $k_{ij..}$(see Appendix C) have the same meanigs as in section 3. In this calculation, we take into account six spieces, as did in section 5. The reactions which we take into account is listed in Appendix C.

6.2 Numerical method

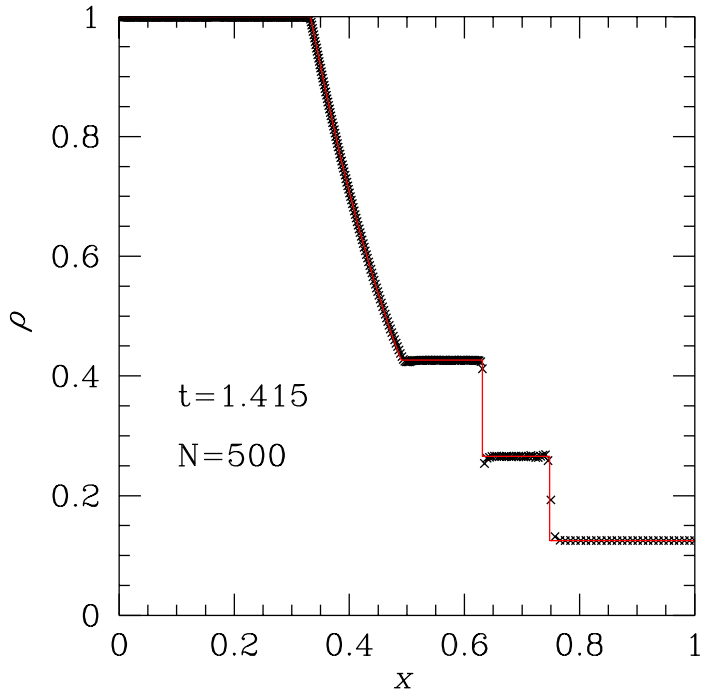

Figure 16: *The snapshot of the density distribution for Sod's problem is presented. The diagonal crosses denote the numerical results by our code, and the solid line denote the analytic solution. The error is less than 1 % for all meshes except at the shock front. The shock front is resolved by at most 3 meshes. In this calculation, the total mesh number is 500.*

We employ the Piecewise Parabolic Method (PPM)(Colella and Woodward 1984 [9]) to calculate the hydrodynamics. The method has two important advantages which are favorable to this calculation. First, this method is a kind of Godonov's method, in which the Riemann's problem is solved between every pair of neighboring mesh. Therefore PPM is very powerful to resolve the shock front. To test the numerical code, the Sod's problem (the shock tube probrem) is solved. The result agrees very well with the analytic solution especially at the shock front (Fig.16). Then we can easily identify the shock front, becase the shock front is almost always represented only one or two meshes. If the shock front is not sharp enough, the radiative cooling or chemical reactions in the trangent region are not negligble, though they are unphysical. The second advantage is due to its Lagrange nature. Before we get to the advantage, the constraint on the mesh number should be

explained. The constraint on the mesh number is due to the thinness of the cooling layer behind the shock front. The length of the cooling layer R_{cool} is expressed as,

$$R_{cool} = v_s t_{cool}, \tag{6. 9}$$

where t_{cool} is the cooling time, v_s is the velocity of the shock front relative to the post shock region. To resolve the cooling layer, we need enough mesh number $\alpha \gtrsim 5 - 10$ in the cooling layer.

$$R_{cool} = \alpha \frac{\Delta m}{\rho}, \tag{6. 10}$$

where α, ρ and Δm denote the mesh number of the cooling layer, postshock density and the colum density per mesh, respectively. On the other hand, the total mesh number N and the mesh size Δm is related to the total colum density of the disk m_0,

$$N\Delta m = \frac{m_0}{2}, \tag{6. 11}$$

The colum density of the disk is related to the total mass and the initial density of the

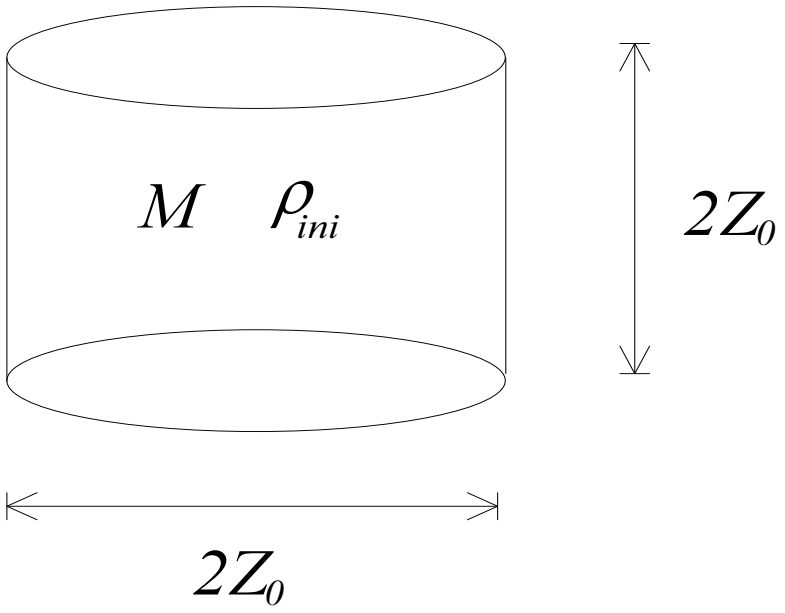

Figure 17: *The initial shape of the cloud is presented.*

cloud, assuming the initial shape of the cloud is a cylinder (Fig.17).

$$\frac{m_0}{2} \simeq \left(\frac{M}{2\pi}\right)^{1/3} \rho_{ini}^{2/3}. \tag{6. 12}$$

The cooling time at $T = 10^4$K is expressed as,

$$t_{cool} = 1.25 \times 10^4 \mathrm{yr}[y_e(1-y_e)/(1+y_e)\rho/m_p]^{-1} \qquad \text{at } T \simeq 10^4\mathrm{K} \qquad (6.\ 13)$$

We estimated the cooling time at $T \sim 10^4$K, because the length of the cooling layer is shortest at this temperature. Combining above four equations (6. 9),(6. 10),(6. 11) and (6. 13) we obtain

$$N = \left(\frac{M}{2\pi}\right)^{1/3} \rho_{ini}^{2/3} \frac{\alpha}{v_s t_{cool} \rho}, \qquad (6.\ 14)$$

$$\simeq 440\alpha (M/10^8 M_\odot)^{1/3} (n_{ini}/1\mathrm{cm}^{-3})^{2/3} (v_s/25\mathrm{km/s})^{-1}. \qquad (6.\ 15)$$

Then if we require to be greater than $5-10$ of α, we need $N \gtrsim 2200 - 4400$. Now in equation (6. 14) show the advantage of PPM method. Because the cooling time is proportional to ρ^{-1}, *N does not depend on the postshock density.* In other words, if the condition $N \gtrsim 2200 - 4400$ is satisfied initially, α is always large enough to resolve the cooling layer. This feature is universal to all Lagrange mesh method for plane parallel configuration.

The chemical reactions (Appendix C) are solved implicitly, because the time scale of the reactions are very short. The radiative cooling in this calculation includes all processes listed in section 2. The optical depth of the cloud is always much smaller than unity for H_2 lines and larger than unity for H lines. Therefore we can use the expression in section 2.

6.3 Initial conditions

The initial conditions and the boundary conditions are listed in Table 6. We test for three mass scales and two different initial density profiles. The boundary coditions for the pressure and the density are set to be constant and very low compared with the initial value of the cloud. The velocity is set to be free at the boundary. We take the initial chemical compositions as the same in section 3 which are the frozen values after the recombination of the universe. The initial temperatures are 100K, and the initial velocities are set to be zero.

6.4 What is expected ?

Now what is expected in the 1-D gravitational collapse of the primordial gas cloud ? In Fig.18, a snap shot of the temperature distribution in 1-D gravitational collpse without any cooling process is presented. In Fig.18 there is a shock front around $m/m_0 \simeq 0.65$ at this time, because we set the initial temperature so low ($T = 100$K) that infall velocity of the cloud is highly supersonic. We also observe that the matter for larger m/m_0 (the spacial coordinate in the Lagrange frame), experience the higher temperature in the postshock region, because the outer region has the higher gravitational potential energy.

On the other hand the important processes corresponding to ranges of the temperature are summarized as follows: 1) for $T \lesssim 3 \times 10^3$K, the radiative cooling due to hydrogen molecules dominates, and the hydrogen molecules form with the catalyst, which is the

Table 6: **Initial Conditions**

Cases	$M/M_\odot$	$n_{ini}\mathrm{cm}^{-3}$	ρ - distribution
A	10^9	2.9	$\rho/\rho_{ini} = 1 + \exp\left(-(2m(z)/m_0)^2\right)$
B	10^8	2.9	
C	10^7	2.9	
D	10^9	10^2	$\rho/\rho_{ini} = 1 + \exp\left(-(2m(z)/m_0)^2\right)$
E	10^8	10^2	
F	10^7	10^2	
G	10^9	2.9	$\rho/\rho_{ini} = 1 + \cos\left(\pi z/z_0\right)$
H	10^8	2.9	
I	10^7	2.9	
A2	10^9	2.9	$\rho/\rho_{ini} = 1 + \exp\left(-(2m(z)/m_0)^2\right)$, No cooling

cosmological residual electron. 2) For $3 \times 10^3\mathrm{K} \lesssim T \lesssim 10^4\mathrm{K}$, the hydrogen molecules dissociate, and the radiative cooling rate becomes inefficient. 3) For $T \gtrsim 10^4\mathrm{K}$, the radiative cooling of hydrogen atom is important and the ionization of the hydrogen atom proceed.

In case the region is heated up to $T \gtrsim 10^4\mathrm{K}$ through the shock heating, the delay of recombination compared to the radiative cooling leaves significant amount of electrons after the temperature drops below $10^4\mathrm{K}$ (section 5). Then the hydrogen molecules are formed with those electrons and the gas cools down to $\sim 200\mathrm{K}$.

Consequently, we can expect the cooled inner region, which never experienced $T \gtrsim 3 \times 10^3\mathrm{K}$ and the relatively hot region just outside the inner cooled layer that has experienced the temperature $3 \times 10^3\mathrm{K} \lesssim T \lesssim 10^4\mathrm{K}$. We also expect the outer cooled region which have experienced $T \gtrsim 10^4\mathrm{K}$. In any case, complex spacial structures are expected.

6.5 Results and discussion

In this section, the results of the hydrodynamical calculations are summarized. We have many models but the basic feature is represented in model A. Therefore the basic results are explained by the results in model A. The model difference is also mentioned at the end of this section.

6.5.1 The oscillation around $T_2 = 10^4\mathrm{K}$

The oscillation of the postshock temperature is seen in Fig.19, and the temperature just behind the shock front decreases. This seems to be quite strange, because the collapsing velocity is the faster for the matter initially placed at the higher point in the gravitational potential well. Accordingly, the temperature just behind the shock always seems to increase as the shock propagate to the outer region. However, checking Fig.20, we can understand what is happing. The most important point in Fig.20 is the increase of *postshock* velocity. This phenomena never happened in the hydrodynamical calculation without any cooling process. The result can be interpreted as follows : the postshock

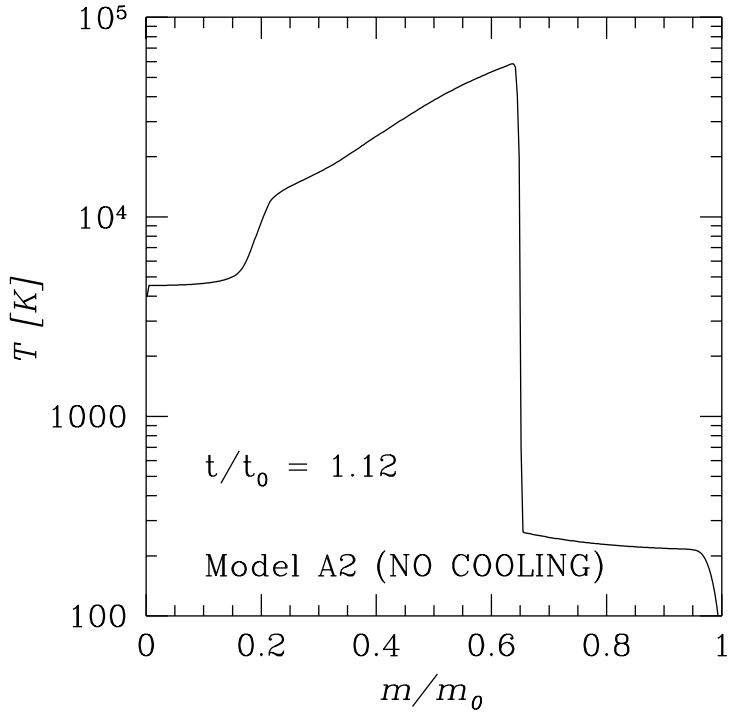

Figure 18: *The snapshot of the temperature distribution of for the colum density $m(z)$ is presented for model A2 which involve no cooling process.*

layer cools so fast that the pressure imbalance cannot be recovered. Then the postshock layer start collaping, followed by the sinking of the shock front. As a result, *the preshock velocity relative to the postshock velocity decreases* and the postshock temperature drops.

Now we present the more detailed argument about this oscillation. The postshock velocity v_2 relative to the midplane of the sheet is nigligible compared to the preshock velocity if the cooling process is negligible. However, when the cooling process is efficient and the pressure balance is kept, the infall velocity v_2 is expressed as,

$$v_2 \sim z_{post}/t_{cool}, \tag{6. 16}$$

where z_{post} denotes the size of the postshock region. This equation shows that the postshock layer shrinks as the thermal energy escapes from the layer. Therefore, if the cooling time is fast enough to satisfy the condition,

$$z_{post}/t_{cool} \gtrsim -v_0, \tag{6. 17}$$

the infall velocity of the postshock layer is not negligible compared to the preshock velocity, where v_0 is the shock velocity measured in the rest frame relative to the z=0 plane. In the above argument, we assume the pressure equilibrium is achieved in the postshock layer. Next, we check this assumption. First of all, the gravity is not important in the postshock layer because the postshock region is highly compressed up to $\sim 10^4 \mathrm{cm}^{-3}$. As a result, the postshock region is not confined with the gravitational force but by the

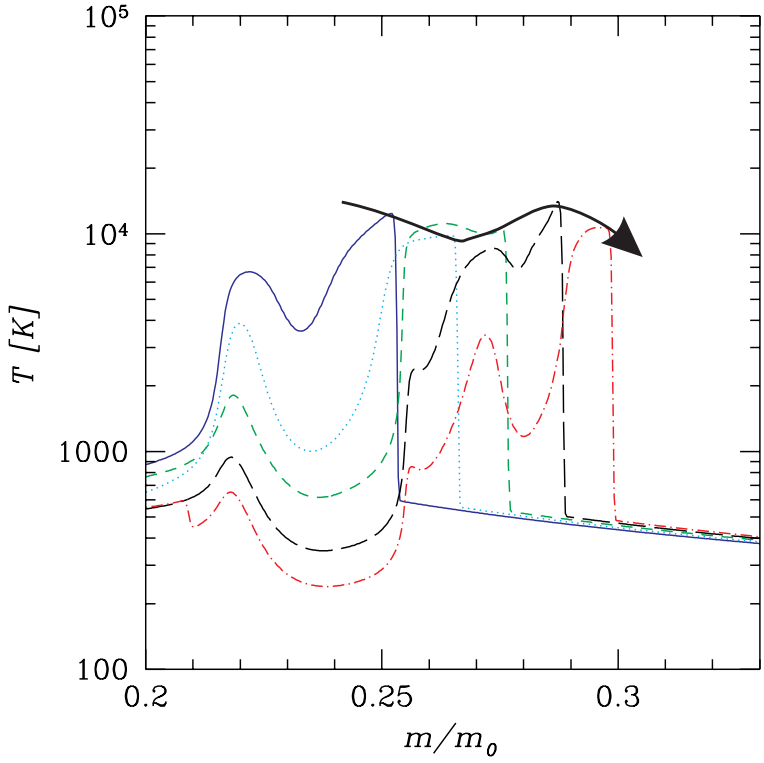

Figure 19: *The temperature distribution of for the colum density $m(z)$ is presented for model A. Many lines corresponding to the time sequence $t\sqrt{4\pi G\rho_{ini}} = 1.028, 1.030, 1.032, 1.034, 1.036$. The arrow connects the temperature just behind the shock at every time sequence. The post shock temperature oscillates as the time proceeds.*

external rampressure. Secondly, we must check whether the sound velocity is fast enough to recover the pressure imbalance produced by any reason. From the jump condition across the strong shock front, we obtain the relation between the temperature just behind the shock and the preshock velocity. It is,

$$kT = \frac{3}{16}\mu m_p (v_1 - v_0)^2, \tag{6. 18}$$

where v_1 denotes the preshock velocity measured in the rest frame relative to the midplane of the sheet. On the other hand, the strong shock condition implies,

$$(v_1 - v_0) = 4(v_2 - v_0), \tag{6. 19}$$

Combining above two equations, we have,

$$(v_2 - v_0) = \sqrt{\frac{kT}{3\mu m_p}}, \tag{6. 20}$$

$$= \frac{c_s}{\sqrt{5}}. \tag{6. 21}$$

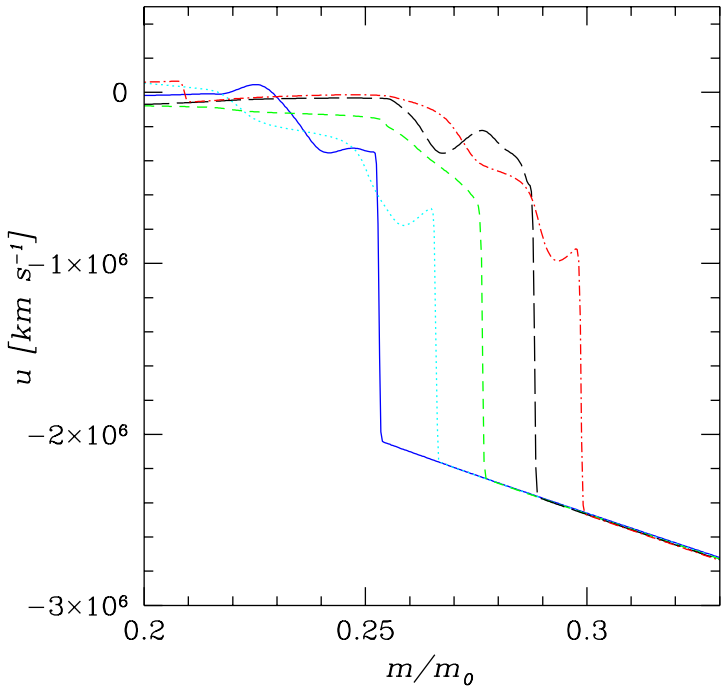

Figure 20: *The velocity distribution of for the colum density $m(z)$ is presented for model A. Many lines corresponding to the time sequence* $t\sqrt{4\pi G\rho_{ini}} = 1.028, 1.030, 1.032, 1.034, 1.036$.

As a consequence, the postshock layer without any cooing process is always isobaric because the sound velocity is faster than the expansion velocity of the postshock layer. However, in case the cooling time is fast enough to satisfy the condition (6. 17), the equations (6. 21)(6. 17) imply,

$$z_{post}/t_{cool} \gtrsim c_s. \tag{6. 22}$$

Therefore, the isobaricity of the cooling layer merginally breaks down. In this case, equation (6. 16) is not valid because it require the pressure balance. In this situation, the infalling velocity of the postshock layer is expressed as,

$$v_2 = f c_s \tag{6. 23}$$

where f is a factor $\sim O(1)$. This expression is obtained from the free expansion of high pressure region surrounded by the low pressure region. Combining equations (6. 18)(6. 19) and (6. 23)) we have,

$$v_0 = -(f - \frac{1}{\sqrt{5}})c_s, \tag{6. 24}$$

$$\frac{v_1}{v_2} = 1 + \frac{3}{f\sqrt{5}}. \tag{6. 25}$$

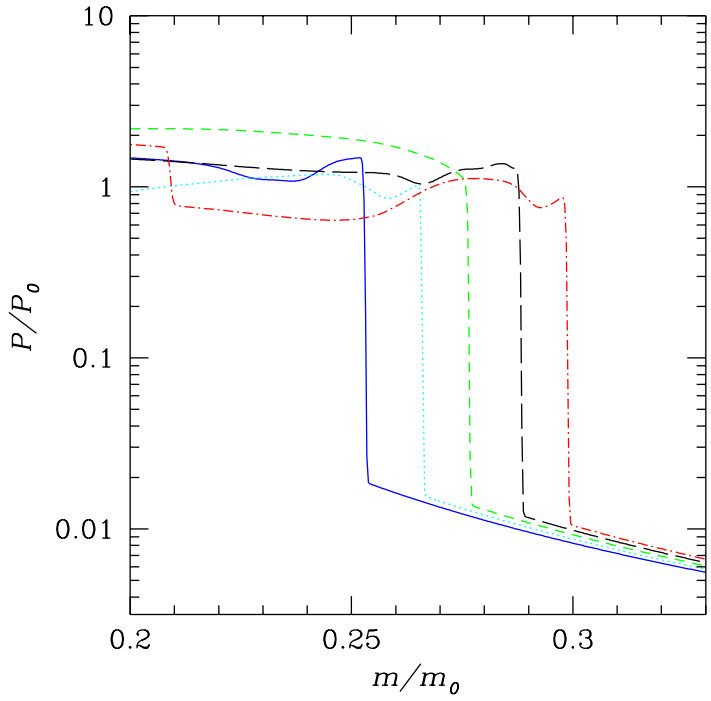

Figure 21: *The pressure distribution of for the colum density $m(z)$ is presented for model A. Many lines corresponding to the time sequence* $t\sqrt{4\pi G\rho_{ini}} = 1.028, 1.030, 1.032, 1.034, 1.036$.

Above results show that the ratio v_1/v_2 has its minimal value $1+3/\sqrt{5} = 2.34$ because the factor f cannot be much above unity. This ratio is consistent with velocity distribution in Fig.20 which is the result of the numerical calculation. In fact, in Fig.21 the cooling layer is not isobaric. We can also find from equation(6. 25) that the shock front "sinks" in Euler coordinate when $f \geq 1/\sqrt{5}$ is satisfied, and it expand when $f \leq 1/\sqrt{5}$. The condition (6. 17) is satisfied when the temperature raise to $\sim 10^4$K, because the cooling time drops significantly due to the Lyman α line cooling and subsequent H_2 vibrational line cooling.

After the condition (6. 17) is satisfied, the postshock temperature drops and the cooling layer recover the pressure balance. Accordingly, the postshock temperature increase again because the infalling postshock velocity become slower again. The same porocess repeat several times. That is why the oscillation sets in around $T \sim 10^4$K in Fig.19. The oscillational porocess stop after the postshock tmperature rise well above $\sim 10^4$K, because the cooling time for higher temperature is less effective than around $T \sim 10^4$K. The cusps corresponding to every oscillation in Fig.19 is due to the different efficiency of the molecular line cooling. The region which has experienced hot stage $T \gtrsim 10^4$K is cooled down to ~ 200K due to the over produced hydrogen molecules (see section 5). On the contrary, the efficiency of the radiative cooling in the region which is heated up to

just below 10^4K is realatively low, because the hydrogen molecules is not produced, but just destroied. Consequently, the cusps are produced with the postshock temperature oscillation around $T \sim 10^4$K.

6.5.2 The time scales

The various time scales in the collapsing disk are presented in Fig.22 for Model A. The figures denoted by (a),(b),(c),(d),(e) and (f) represent the history of the spacial distributions of the time scales. The four lines denote the cooling time (t_{cool}), the sound crossing time (t_{sound}), the free-fall time (t_{ff}) and the dynamical time (t_{dyn}). The correspondence of each line with the above four time scales are explained in the figure caption. The definitions of the time scales are as follows:

$$t_{cool} = \frac{3}{2} nkT/\Lambda(\rho, T, y_i), \tag{6. 26}$$

$$t_{sound} = \frac{z(m)}{c_s}, \tag{6. 27}$$

$$t_{ff} = \frac{1}{\sqrt{4\pi G\rho}}, \tag{6. 28}$$

$$t_{dyn} = \frac{z(m)}{v(m)}, \tag{6. 29}$$

where $z(m)$ and $v(m)$ denote the height and the velocity of the point at which the time scales are measured. Now first of all, we reexamin the results mensioned in the previous subsection. It is mensioned that the factor f is $\sim O(1)$, which means the dynamical time scale of the postshock region is comparable to the sound crossing time. In fact, $t_{dyn} \simeq t_{sound}$ is roughly satisfied in the narrow cooling layers in several figures in Fig.22. Next, we compare the dynamical time scale and the free-fall time. Following the time sequence from (a) to (f), t_{dyn} is much smaller than t_{ff} in the whole region ((a)-(b)), then t_{dyn} becomes comparable with t_{ff} in the postshock region ((c)-(d)), and finally t_{dyn} get larger than t_{ff} in the cooling layer ((e)-(f)). *If we regard the free-fall time as the time scale of maximum growth rate of the density perturbations across the sheet, the postshock layer of the sheet will fragment into many cylinders at the epoch denoted by (c) or (d).* After this first fragmentation, the subsequent cylinderical collapse sets in (section 4).

On the other hand, we perform the numerical calculations for one zone cylinderical collapse for various initial conditions (section 4) and we obtain the contour map of the fragment mass scale (Fig.25).

For expample, the initial condition for the cylinderical collapse is obtained form Fig.22(d) and other corresponding figures (Fig.23, Fig.24) in model A. In this model, the initial conditions for the cylinderical collapse are, $n \simeq 10^4 \mathrm{cm}^{-3}$ and $T \simeq 200 - 300$K. The chemical compositions are $y_e = 10^{-2}, y_{H^-} = 10^{-13}, y_{H_2} = 10^{-3}$. Therefore, the mass of the fragment at the end of the cylinderical collapse is obtained from the contour map (Fig.25),

$$M_{frag} \sim 10^3 M_\odot \qquad for \quad modelA. \tag{6. 30}$$

This value is much larger than the *Chandraskhar mass* limit obtained in sention 4, because the temperature is too low to cool the filaments dynamically. The collapse stops at rather

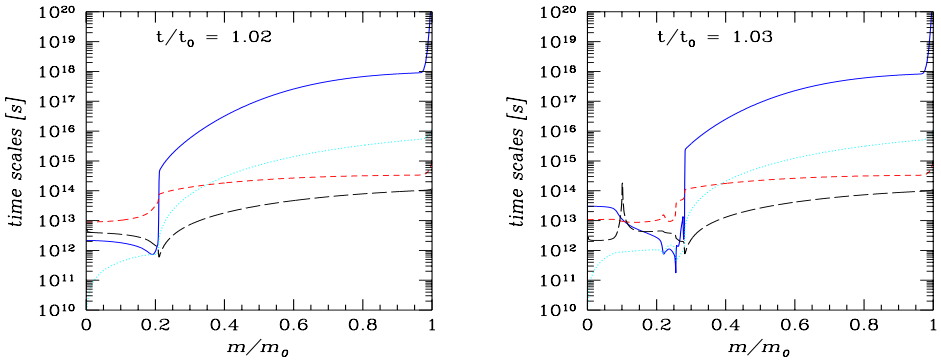

(a) $t = 1.02$ (b) $t = 1.03$

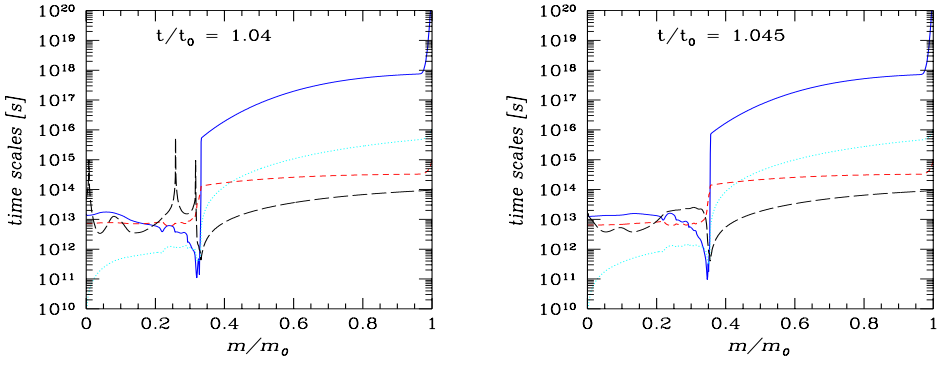

(c) $t = 1.04$ (d) $t = 1.045$

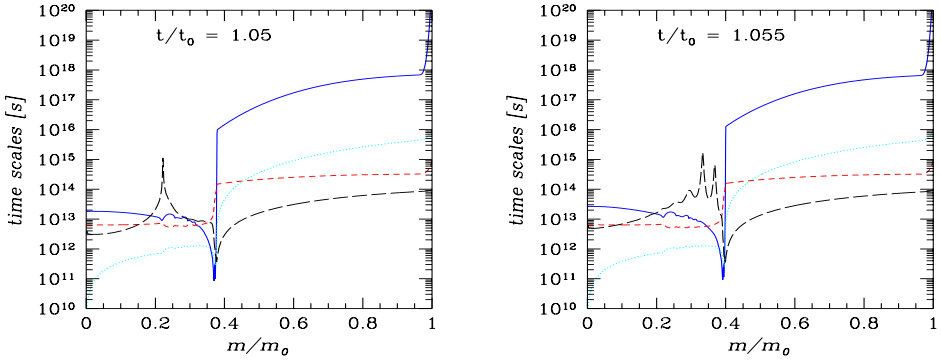

(e) $t = 1.05$ (f) $t = 1.055$

Figure 22: *The time scales are presented for different epochs in model A. The solid lines represent t_{cool}, the dotted lines represent t_{sound}, the short-dased lines represent t_{ff} and the long-dashed lines represent t_{dyn}. The horizontal axis is the colum density of the cloud measured from the midplane of the sheet and it is normalized by the total colum density.*

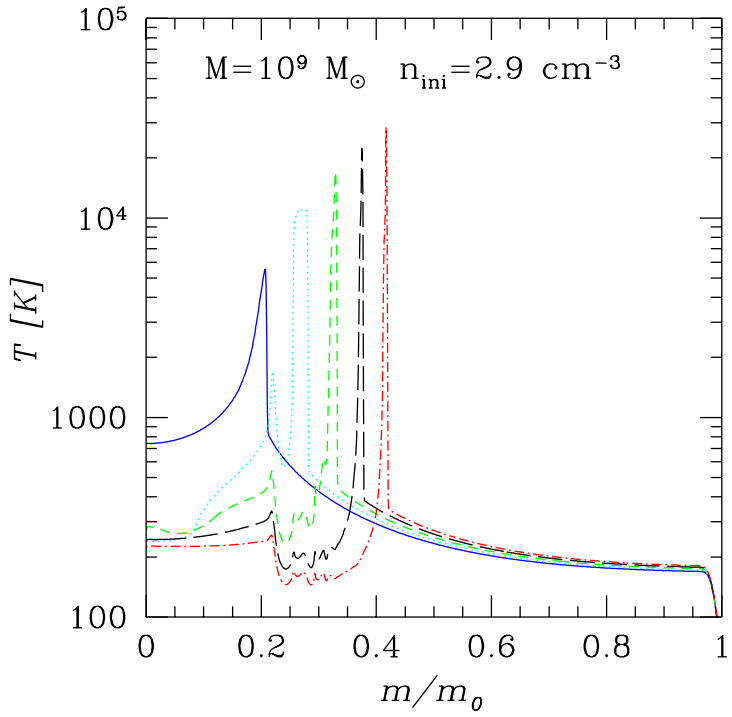

Figure 23: *The temperature distribution in the Lagrange coordinate is presented for several time sequence. The solid line, the dotted line, the short dased line, the long dased line and the dot-short dased line denote the* $t/t_0 = 1.02, 1.03, 1.04, 1.05$ *and* 1.06.

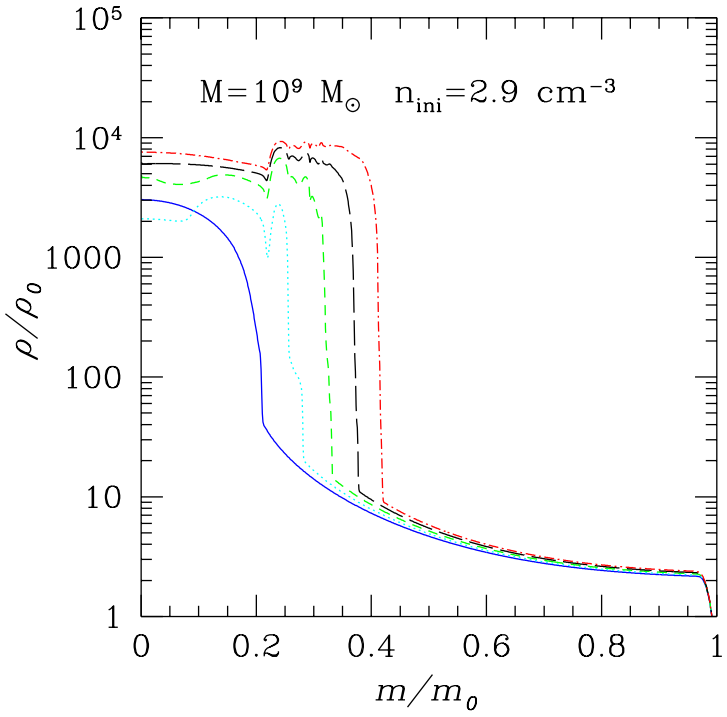

Figure 24: *The density distribution in the Lagrange coordinate is presented for various epochs. The correspondence of the lines and the time is the same as in Fig.23.*

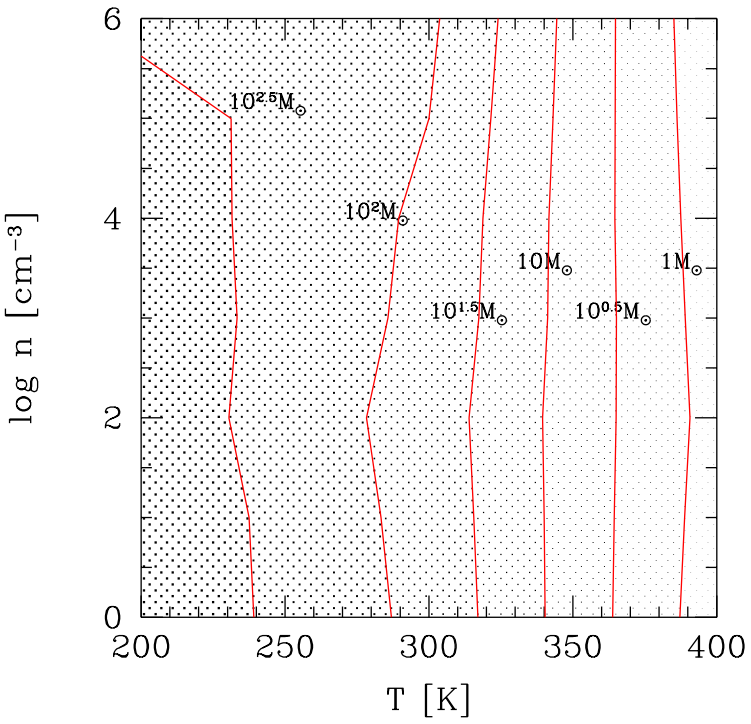

Figure 25: *The mass of the fragment in the cylinderical collapse is presented for various initial densities and the temperatures. Other initial conditions are fixed as* $y_e = 10^{-2}, y_{H^-} = 10^{-13}, y_{H_2} = 10^{-3}$. *The line density of the cylinders are set to be 2 times greater than the critical line density* $2kT/(\mu m_H G)$ *as in the case E in table 5. The numerical calculations are performed in the same way as in section 4.*

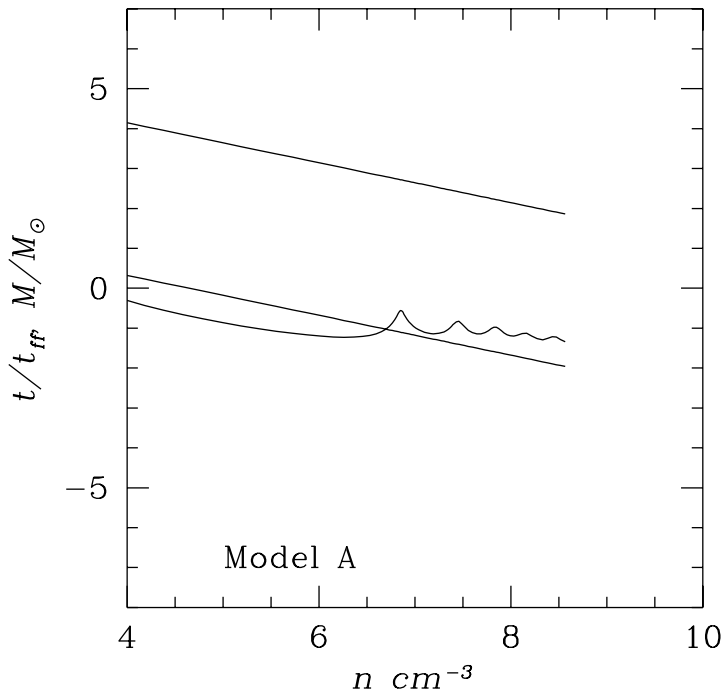

Figure 26: *The evolution of the time scales in the one zone cylinder colapse for the initial condition obtained from the Model A.*

Table 7: **The Mass of the Fragment for Various Initial Cylinder**

T [K]	n [K]	$lnM_{frag}/M_{\odot}$
200	1	2.9
	10	2.9
	10^2	2.8
	10^3	2.8
	10^4	2.8
	10^5	2.7
	10^6	2.4
300	1	1.9
	10	1.8
	10^2	1.8
	10^3	1.9
	10^4	1.9
	10^5	2.0
	10^6	2.1
400	1	-0.27
	10	-0.23
	10^2	-0.18
	10^3	-0.23
	10^4	-0.27
	10^5	-0.32
	10^6	-0.36

Table 8: **The Mass of the Fragment for Various Models**

Model	$T_{\rm sheet\to cylinder}$[K]	$n_{\rm sheet\to cylinder}[{\rm cm}^{-3}]$	$M_{frag}/M_\odot$	fraction of the fragments
A	$2\times10^2-3\times10^2$	$6\times10^3-9\times10^3$	10^2-10^3	3.5×10^{-1}
B	$2\times10^2-4\times10^2$	$1\times10^3-2\times10^3$	$1-10^3$	6×10^{-1}
C	$8\times10^2-1\times10^3$	$9\times10-1\times10^2$	~ 1?	5×10^{-1}
D	$5\times10^2-6\times10^2$	$8\times10^5-9\times10^5$	~ 1?	1.5×10^{-1}
E	$5\times10^2-6\times10^2$	$1\times10^5-2\times10^5$	~ 1?	2.5×10^{-1}
F	$3\times10^2-6\times10^2$	$5\times10^4-2\times10^5$	$1?-10^2$	7×10^{-1}
G	$2\times10^2-3\times10^2$	$7\times10^3-1\times10^4$	10^2-10^3	4×10^{-1}
H	$4\times10^2-5\times10^2$	$1\times10^3-2\times10^3$	~ 1?	4×10^{-1}
I	$1\times10^3-3\times10^3$	$2\times10^1-7\times10^1$	~ 1?	8×10^{-1}

low density (Fig.26) than in section 4. Then the fraction of hydrogen molecules do not grow to $\sim O(1)$ because the key reactions (three-body reactions) to produce hydrogen molecules are not important at low density ($n \lesssim 10^8{\rm cm}^{-3}$). As a result, the assumption to derive the Chandrasekhar mass breaks down in this case. Anyway, the postshock cooling layer will fragment into many cylinders at the time that the condition $t_{dyn} \sim t_{ff}$ is satisfied, and the cylinders fragment into smaller clumps $\sim 10^3 M_\odot$. In this model, the total mass of the fragment is about 35 % of the sheet (Fig.23). We also hope to obtain the infomation about the rest of the gas. Unfortunately, the fate of the preshock gas cannot be predicted precisely in this calculation because it is not valid after the postshock gas fragment. However, in the next section (section 7) some discussions are presented for the preshock gas.

6.5.3 The model difference

Adopting the same procedure for other models, we obtain the mass of the fragments for other models. In table 8, the mass of the fragments and the initial conditions for the cylinderical collapse are listed. In table 8, all quantities have ambiguities, because those have the spacial distribution.

For model A, the mass of the fragment is very large compared with the Chandrasekhar mass. However, in model B, the mass scale drops eventually, to $\sim 1 M_\odot$ if we take the maximal initial temperature, $T_{\rm sheet\to cylinder}$. This difference is due to the temperature when the postshock layer of the sheet fragment into cylinders. In model A, the temperature is $\sim$ 200K, below which the cooling rate exponentially drops down. Accordingly, the cylinder cannot collapse so fast that the final fragmentation (cylinder $\to$ clumps) occur at low density. On the other hand, the temperature is $\sim$ 400K in model B. In this case, the cloud can cool down to lower temperature, resulting the final fragmentation at higher density ($\gtrsim 10^{10}{\rm cm}^{-3}$) above which the assumption to derive the Chandrasekhar mass in section 4 holds. Unfortunately in model C, the final fragment mass cannot be estimated because of the limitation of one zone approximation employed in the calculation of cylinder collapse (section 4). In this case, the temperature at the first fragmentation (sheet $\to$

cylinder) is so high $\gtrsim$ 700K that the final temperature (four times larger than the initial temperature) is above the dissociation limit ($\sim$ 2000K) of hydrogen molecules. As a consequence, the assumption to derive the Chandrasekhar mass breaks down. However, according to Nakamura (1996) [38], who have performed hydrodynamical calculations on 1-D cylinderical collapse of primordial gas clouds, a cool cylinderical core which consists of hydrogen molecules form at the center of the cylinder though the outer envelope is so hot that the hydrogen molecules dissociate. If we admit his results, the core of the cylinder fragment into small clumps with $M \sim 1M_{\odot}$.

The difference among the values of $T_{\rm sheet\rightarrow cylinder}$ for different models A, B and C, are simply due to the mass scale (colum density) of the sheets. For higher mass scales, the rampressure is so high that the inner region is compressed to higher density than the one in lower mass clouds. Therefore, the cooling time which is proportional to ρ^{-1} gets shorter compared to the free fall time, which is proportional to $\rho^{-1/2}$. On the other hand, the dynamical time near the mid plane of the disk is almost determined by the cooling time. As a result, the fragmentation of a sheet to cylinders sets in at larger density and lower temperature for larger mass in case initial density of the sheet (n_{ini}) is 2.9cm^{-3}.

However, in the models D, E and F the situations are differnt from that of the model A, B, and C. In D, E and F initial densities of the sheets are set to be 10^2cm^{-3}, which are greater than the one in previous models. As seen in table 8, the final mass of the fragments and the initial temperature of the cylinderical collapse have oppisite dependence on M compared with A, B and C. The nature of the molecular cooling time scale, which is explained in subsection 2.5 is responsible for this phenomena. As was explained in subsection 2.5, the cooling rate due to the excitation of hydrogen molecules changes its dependence on density at the *critical density*, which is $\sim 10^4$cm^{-3}. As a result, the cooling time also changes its dependence on density at the critical density as follows:

$$\begin{aligned} t_{cool} &\propto \rho^{-1} \qquad \rho < \rho_{cr}, \\ t_{cool} &\propto \rho^{0} \qquad \rho > \rho_{cr}, \end{aligned} \tag{6. 31}$$

where ρ_{cr} is the critical mass density of molecular line cooling. Therefore, the ratio t_{cool}/t_{ff} decreases as the compression proceeds for $\rho > \rho_{cr}$. Hence, at high density, the dynamical time (cooling time) at the inner cooled region becomes comparable with the free-fall time at rather high temperature. In other words, the fragmentation proceeds faster than the cooling processes. In model D and E, the densities at the inner cooled regions exceed critical density. Consequently, the sheets fragment into cylinders at rather high temperature compared with the model F. We also mention that the initial temperatures of the cylinderical collapse for model A and B are smaller than those in model D and E. This is simply due to the difference on the initial densities of sheets. In model A and B, the central density do not exceed the critical density, though those in model D and E do. Accordingly, the same argument for the difference between D,E and F can be applied to this difference.

The models G, H and I are diffrent from A, B and C for their initial spacial distribution of density. As shown in table 8, the differences between A ,B, C and G, H, I on $T_{\rm sheet\rightarrow cylinder}$ and $n_{\rm sheet\rightarrow cylinder}$ seem to be small. This result implies that initial distribution of the density do not affect the evolution of the central layer unless the distribution is an eccentric one.

7 Summary

In this thesis, the thermal evolution of primordial gas clouds which have formed out of initial density perturbations in the early universe is investigated. Rough estimates are presented using the one zone models in section 3 and section 4.

In section 3, the collapse of the spheroids are investigated to include the effects of the anisotropy of the density perturbations. The initial anisotropy of primordial clouds are enhanced by the nature of gravity. In case the initial clouds are oblate, the clouds become a thin disk. The different dependence on the density between the time scale of disk collapse and that of spherical one, the clouds trace different evolutionary paths on the $n-T$ diagram. The angular momentum also affects the evolution of the clouds since there exist angular momentum barriers. The clouds which rotate fast enough, evolve as the oblate clouds. The mass of the fragments are estimated by the thickness of the disks. The mass is expected much higher ($M \sim 10^2 M_\odot$) than the ordinary stellar mass scale. However, this treatment contained several problems. First of all, the collapse of cool clouds such as the cosmological density perturbations in galactic scales proceed in a very dynamical way, and the strong shocks are expected. On this problem, section 5 and section 6 are devoted. Secondly, the mass of the fragments are estimated at the condition

$$t_{ff} = t_{sound}, \tag{7.1}$$

is satisfied. However, the fragmentation seems to occur when the condition

$$t_{ff} \simeq t_{dyn}, \tag{7.2}$$

is satisfied, and this condition is fulfilled later than the previous condition. Finally, due to the nature of gravity, the sheets fragment into many cylinders rather than clumps. Therefore the fragmentation of cylinders must be investigated.

In section 4, the collapse of infinitely long cylinders are investigated with one zone models. Since the cylinderical collapse is relatively quiet compared with the disk collapse, we have taken into account the pressure gradient force, though the one zone models are employed. As a result, we can test the condition (7. 2). It is found that the final fragment mass of cylinders is essentially determined by the virial temperature of the cylinders, which depends just on the line densities. For larger line densities, the cylinders fragment into heavier clumps, and for smaller line density, they fragment into lighter clumps. It is also found that there exists a minimal value of the mass of the fragments both numerically and analytically. The lower limit is determined by the Chandrasekhar mass times a factor which is $O(1)$.

Following these works related with one zone models, we proceed to the investigation on the spatial structure of primordial gas clouds. In section 5, we examined the thermal evolution of the postshock layer in a steady flow. Since this problem is already investigated by SK numerically, we tried a semi-analytical approach to let the physics of postshock layer be much clear. We found that the thermal evolution of the postshock layer is easily understood by the $y_e - T$ diagram (Fig. 13). The $y_e - T$ plane is divided by the lines $t_{cool} = t_{ion}$ and $t_{rec} = t_{cool}$ and the system evolve along with the arrows presented in Fig.13.

In the gravitational collapse of a disk, however, much more complicated structures are expected due to the different initial potential energy for different fluid elements. In section 6, we performed the hydrodynamical calculations of initially cool disks, coupled with the radiative cooling and the chemical reactions. We found that an oscillation of the postshock temperature at $T \sim 10^4$K because of the rapidness of the cooling processes in the postshock layer. We also found that the fragmentation of the disk sets in at the inner region. The cooled region fragments into many cylinders, whose line densities are determined by the temperature of the cooled region. In low density models (A, B and C), the initial temperature for the collapse of cylinders become larger for heavier sheets. Nevertheless, in the models whose initial density of the disk is high enough for the central density to exceed the critical density of molecular cooling, the heavier sheets fragment at higher temperature. In our calculation, the range of final fragment mass scales for various models is $1M_\odot \lesssim M \lesssim 10^3 M_\odot$.

However, the estimation of fragment mass scales contains many ambiguities . 1)The ratio of the line density of a cylinder to the temperature is set to be 2 in section 6, though it affects the final fragment mass greatly (section 4). In addition to this fact, the final mass of the fragments have very sharp dependence on the initial temperature (Fig.25). 2)Since the sheets have very complicated spatial structures, we do not know whether the simple theory of fragmentation of sheets are valid or not.

We also have to investigate the necessities of the outer envelops of the sheets which do not fragment at first. The outer envelopes have very high shock velocities which can easily ionize all hydrogen atoms in our model A and B (section6). After the fragmentation of inner cooled region occurred, the fluid elements will be shock heated at the midplane of the sheet. Then a cool layer may emerge again, since the delay of recombination compared with the radiative cooling may produce enough hydrogen molecules (section 5).

To answer those problems we may need higher dimensional hydrodynamical calculations.

Acknowledgments

I am grateful to R.Nishi checking part of this thesis and giving me important suggestions. I thank H.Uehara who is a collaborator of our work on the formation of galaxies, for the calculations of one zone cylinderical collapse in section 4 and section 6. I thank S.Inutsuka, M.Umemura and N.Gouda for useful discussions in the local meeting of galaxy formation. I thank Y.Yamada for critical discussions on numerical methods. I would like to thank H.Sato and T.Nakamura introducing me to rich and interesting world of astrophysics. I thank to N.Sugiyama and M.Siino giving me their rich knowledge of English. I also thank K.Yokota who is the secretary of our department for every kind of supports. Finally, I thank to all members in our laboratory TENTAIKAKU for heartful supports and continuous encouragement. This work was supported in part by the Monbusho Grant-in-Aid for Scientific Research Fund, No.3077.

APPENDIX

A H_2 line cooling (the expression for general value of τ for the one zone model)

Hydrogen molecules have many excited levels corresponding to the vibrational and rotational quantum states. The radiative transition from a higher energy level to a lower energy level of a hydrogen molecule results in cooling of the cloud, if the emitted photon escapes from the cloud. We have to estimate the level populations of H_2, so that we can calculate the emissivity j_ν [$\mathrm{erg \cdot s^{-1} \cdot cm^{-3} Hz^{-1} str^{-1}}$]. The level populations are determined by the statistical equilibrium of the transitions between those states. To know the level populations, we need the Einstein's A coefficients between the levels, and also need the collisional excitation rates. We take those values from Hollenbach et.al (1979) and Turner et.al.(1977), respectively. We neglect the absorption and the stimulated emission, because those effects do not change the level population in this calculation. Once we know the level populations, we can give the emissivity of the energy transition as follows:

$$j_\nu = \Delta E_{i \to j} A_{ij} n_i \frac{\phi(\nu)}{4\pi}, \tag{A.1}$$

where $\Delta E_{i\to j}, A_{ij}, n_i$ and $\phi(\nu)$ denote the energy difference of the two states, the Einstein's A coefficient, the number density of the ith state of H_2 and the line profile function. In our calculation, the profile is determined by the Doppler broadening. Using this emissivity and the level populations, we can solve the radiative transfer equation for a line emission. The derivation of the cooling function is shown in the Appendix B.

B Radiative Transfer

Here we show the solution of the radiative transfer equation in the case of a uniform sphere, a uniform disk and a uniform cylinder. Then the derivation of the cooling function due to the line cooling is shown. First, the radiative transfer equation along the s-direction is as follows:

$$\frac{dI_\nu}{ds} = -k_\nu I_\nu + j_\nu, \tag{B.1}$$

where I_ν, k_ν, j_ν denote the intensity of the radiation, the opacity, and the volume emissivity, respectively. This equation is formally integrated,

$$I_\nu(\tau(\nu)) = I_\nu(0) e^{-\tau(\nu)} + \int_0^{\tau(\nu)} e^{-(\tau(\nu)-\tau')} S_\nu(\tau') d\tau', \tag{B.2}$$

where,

$$S_\nu \equiv j_\nu / k_\nu, \quad \tau(\nu) \equiv \int_0^s k_\nu ds. \tag{B.3}$$

If the cloud is uniform, k_ν, j_ν and S_ν must be constant along any line of sight. Then, the solution is simplified as follows.

$$\tau(\nu) = k_\nu s \tag{B. 4}$$

$$I_\nu(\tau(\nu)) = S_\nu + e^{-\tau(\nu)} (I_\nu(0) - S_\nu) \tag{B. 5}$$

Now we can calculate the energy flux radiated from a uniform sphere. The energy flux is given in terms of the intensity,

$$F_\nu = \int d\Omega I_\nu(\theta, \varphi) \cos\theta. \tag{B.6}$$

In case we treat a uniform sphere, the above integration can be performed easily with the boundary condition $I_\nu(0) = 0$, and the final result is as follows:

$$F_\nu = \pi S_\nu \left(1 + \frac{e^{-2\tau_{tot}(\nu)}\left(1 + 2\tau_{tot}(\nu)\right) - 1}{2\tau_{tot}(\nu)^2}\right), \tag{B.7}$$

where, $\tau_{tot}(\nu) = k_\nu R$, and R denotes the radius of the uniform sphere. Then, we can estimate the cooling function $\Lambda_{rad}(\nu)[\,\mathrm{erg}\cdot\mathrm{s}^{-1}\cdot\mathrm{cm}^{-3}\cdot\mathrm{Hz}^{-1}]$ to be,

$$\Lambda_{rad}(\nu) = \frac{3F_\nu}{R}. \tag{B.8}$$

This treatment is different from PSS, in which they regard the cooling rate more approximately as follows: for $\tau < 1$, they calculate the cooling rate by assuming that all radiation emitted from the gas can escape to the outside of cloud, and for $\tau > 1$, they estimate the flux radiated from the surface of the cloud by the Planck distribution times Doppler width. The difference between our treatment and that of PSS is significant at $\tau \simeq 1$. It should be noted that a significant fraction of the total emitted energy is radiated away especially from the cloud around $\tau \simeq 1$.

We also can integrate the radiative transfer equation for a planar cloud. Performing the integration $(B.6)$ for the planar geometry, we obtain the expression for F_ν . In this case, F_ν can be written analytically using the 1st exponential function,

$$F_\nu = \pi S_\nu \left(\left(1 - e^{-\tau_{tot}(\nu)}\right)\left(1 - \tau_{tot}(\nu)\right) + \tau_{tot}(\nu)^2 E_1\left(-\tau_{tot}(\nu)\right)\right), \tag{B.9}$$

where $E_i(x)$ is the 1st exponential integration,

$$E_1(x) \equiv -\int_{-x}^{\infty} \frac{e^{-t}}{t} dt \quad (for\ x < 0). \tag{B.10}$$

The $\tau_{tot}(\nu)$ in the above equation is redefined as,

$$\tau_{tot}(\nu) \equiv k_\nu Z, \tag{B.11}$$

where Z denotes the thickness of the disk.

Then we approximate F_ν as the flux radiated from a geometrically thin disk. This approximation is valid if the disk is thin enough. Then the cooling function $\Lambda_{rad}(\nu)$ is calculated as follows.

$$\Lambda_{rad}(\nu) = \frac{2F_\nu}{Z}. \tag{B.12}$$

If the cloud can be approximated as an infinitely long cylinder, we can calculate $\Lambda_{rad}(\nu)$. Although it cannot be expressed analytically, we have an empirical expression as

$$\begin{aligned} F_\nu &= S_\nu \left(\pi - \int_0^{2\pi} d\varphi \int_0^{\pi/2} d\theta \sin\theta \cos\theta \exp\left(-\tau_{tot}(\nu) \frac{\cos\theta}{\cos^2\theta + \sin^2\theta \sin^2\varphi} \right) \right) \\ &= S_\nu f\left(\tau_{tot}(\nu)\right), \qquad \text{(B. 13)} \\ \tau_{tot}(\nu) &\equiv 2k_\nu R, \qquad \text{(B. 14)} \end{aligned}$$

where

$$\begin{aligned} f(x) &= 2\pi(x - \frac{2}{3}x^2) \qquad (\text{for } x < 0.01), \\ &= \mathrm{dex}\,[\, 0.40793 + 0.308611y - 0.344113y^2 \\ &\qquad +0.0673944y^3 + 0.057328y^4\,] \qquad (\text{for } y = \log_{10} x \;\; 0.01 \le x \le 10), \\ &= \pi \qquad (\text{for } 10 < x), \end{aligned} \qquad \text{(B.15)}$$

and R denotes the radius of the cylinder. These expressions are obtained by fitting the numerically integrated solution. In this case, the cooling function is expressed as,

$$\Lambda_{rad}(\nu) = \frac{2F_\nu}{R}. \qquad \text{(B. 16)}$$

Once we know the expression of $\Lambda_{rad}(\nu)$, we can also calculate the cooling rate integrated over the frequency. The cooling rate due to the line emission of hydrogen molecules, $\Lambda_{rad}[\,\mathrm{erg \cdot s^{-1} \cdot cm^{-3}}]$ is expressed as follows:

$$\Lambda_{rad} = \sum_{i,j} \Lambda_{rad}(\nu_{ij}) 2f \Delta\nu_D, \qquad \text{(B.17)}$$

where $\Delta\nu_D$ denotes the line width determined by the Doppler broadening. We set the factor f unity, because it is always close to unity. In the optically thin limit f equals to $\sqrt{\pi}/2$, though it is very close to unity for the optically thick limit unless the Lorenzian wing contribute the total emission significantly.

C The chemical reactions

Here, the chemical reactions which we employ in section 5, and section 6 are listed in table 9.

D Steady shock

In this section, the basic equations of the steady shock are presented. SK solved these equations coupled with the chemical reactions. One of the most important feature of the steady shock is the isobaricity of the postshock layer.

Table 9: **The chemical reactions**

Reactions	Rate Coefficients	Refference
$H^+ + e \rightarrow H + \gamma$	k_1 see section 2	[56]
$H + e \rightarrow H^- + \gamma$	$k_2 = 1.0 \times 10^{-18} T \mathrm{cm^3 s^{-1}}$ $T < 1.5 \times 10^4 \mathrm{K}$	[10]
	$= \mathrm{dex}(-14.10 + 0.1175 \log T - 9.813 \times 10^{-3} (\log T)^2) \mathrm{cm^3 s^{-1}}$	
	$T > 1.5 \times 10^4 \mathrm{K}$	
$H^- + H \rightarrow H_2 + e$	$k_3 = 1.3 \times 10^{-9} \mathrm{cm^3 s^{-1}}$ $T < 10^4 \mathrm{K}$	[3]
	$= \mathrm{dex}(-8.78 + 0.113 \log T - 3.745 \times 10^{-2} (\log T)^2) \mathrm{cm^3 s^{-1}}$	
	$T > 10^4 \mathrm{K}$	
$3H \rightarrow H_2 + H$	$k_4 = 5.5 \times 10^{-29} T^{-1} \mathrm{cm^6 s^{-1}}$	[40]
$H_2 + H \rightarrow 3H$	k_5 see section 2	[50]
$2H + H_2 \rightarrow 2H_2$	$k_6 = k_4 / 8 \mathrm{cm^6 s^{-1}}$	[40]
$2H_2 \rightarrow 2H + H_2$	k_7 see section 2	[50]
$H + e \rightarrow H^+ + 2e$	$k_8$see section 2	[29]
$2H \rightarrow H + H^+ + e$	$k_9 = 1.7 \times 10^{-4} k_8$	[40]
$H + H^+ \rightarrow H_2^+ + \gamma$	$k_{10} = 1.85 \times 10^{-23} T^{1.8} \mathrm{cm^3 s^{-1}}$ $T < 6.7 \times 10^3 \mathrm{K}$	[45]
	$= 5.81 \times 10^{-16} (T/56200)^{-0.6657 \log (T/56200)} \mathrm{cm^3 s^{-1}}$	
	$T > 6.7 \times 10^3 \mathrm{K}$	
$H_2^+ + H \rightarrow H_2 + H^+$	$k_{11} = 6.0 \times 10^{-10} \mathrm{cm^3 s^{-1}}$	[23]
$H_2 + H^+ \rightarrow H_2^+ + H$	$k_{12} = 2.4 \times 10^{-9} \exp(-21200/T) \mathrm{cm^3 s^{-1}}$	[43]
$H^- + H^+ \rightarrow H_2^+ + e$	$k_{13} = 1.0 \times 10^{-8} T^{-0.4} \mathrm{cm^3 s^{-1}}$ $T < 10^4 \mathrm{K}$	[42]
	$4 \times 10^{-4} T^{-1.4} \exp(-15100/T) \mathrm{cm^3 s^{-1}}$ $T > 10^4 \mathrm{K}$	
$H_2^+ + e \rightarrow 2H$	$k_{14} = 2.25 \times 10^{-6} T^{-0.5} \mathrm{cm^3 s^{-1}}$	[34]
$H_2^+ + H^- \rightarrow H + H_2$	$k_{15} = 4 \times 10^{-6} T^{-0.5} \mathrm{cm^3 s^{-1}}$	[43]
$H^- + e \rightarrow H + 2e$	$k_{16} = 4 \times 10^{-12} T \exp(-8750/T) \mathrm{cm^3 s^{-1}}$	[12]
$H^- + H \rightarrow 2H + e$	$k_{17} = 5.3 \times 10^{-20} T^{2.17} \exp(-8750/T) \mathrm{cm^3 s^{-1}}$	[22]
$H^- + H^+ \rightarrow 2H$	$k_{18} = 4 \times 10^{-6} T^{-0.5} \mathrm{cm^3 s^{-1}}$	[12]

D.1 Basic equations

The jump conditions at the shock front are,

$$\rho_1 v_1 = \rho_2 v_2 \tag{D. 1}$$

$$\rho_1 v_1^2 + p_1 = \rho_2 v_2^2 + p_2 \tag{D. 2}$$

$$v_1 \left(\frac{\rho_1 v_1^2}{2} + \frac{\gamma_1}{\gamma_1 - 1} p_1 \right) = u_2 \left(\frac{\rho_2 v_2^2}{2} + \frac{\gamma_2}{\gamma_2 - 1} p_2. \right) \tag{D. 3}$$

These equations are the conservation law of the mass, momentum and the energy across the shock front. The quantities whose suffixes are 1 and 2 denote the hydrodynamical variable in the preshock region and the postshock region. In case the shock is strong, i.e. the sound velocity in the preshock region is much smaller than the bulk velocity u_1, we obtain from equations (D. 1),(D. 2) and (D. 3),

$$\rho_2/\rho_1 = v_1/v_2 = 4, \tag{D. 4}$$

$$kT = \frac{3}{16} \mu m_p v_1^2, \tag{D. 5}$$

where μ and m_p are the mean molecular weight of the gas and proton mass.

Behind the shock front, the assumption that the flow is steady allow us to write the conservation of mass, momentum and the energy as follows:

$$\rho v = \rho_2 v_2, \tag{D. 6}$$

$$\rho v^2 + p = \rho_2 v_2^2 + p_2, \tag{D. 7}$$

$$\frac{dE}{dt} = (\Gamma - \Lambda) + [(p + E)] \frac{1}{\rho} \frac{dE}{d\rho}, \tag{D. 8}$$

where Γ , Λ and E denote heating and cooling rates, and internal energy per unit volume, and d/dt is Lagrange derivative. The hydrodynamical variables with no suffix denote the quantities at general point behind the shock front. In addition, we require the equation of state $p = nkT$. Then the equations are closed and we can solve the flow equations.

D.2 Isobaricity of the postshock layer

The assumption that the flow is steady indicate the isobaricity of the postshcok region. From equations (D. 7),(D. 8) and the equation of state, $p = \rho kT/(m_p \mu)$, the relative compression factor $x \equiv \rho/\rho_2$ is given by,

$$\frac{kT}{m_p \mu} x^2 - (1 + \frac{p_2}{\rho_2 v_2^2}) x + v_2^2 = 0. \tag{D. 9}$$

In case the shock is strong, the above equation becomes,

$$\frac{kT}{m_p \mu} x^2 - 4 v_2^2 x + v_2^2 = 0. \tag{D. 10}$$

The solution exists if the condition

$$v_2^2(4v_2^2 - \frac{kT}{m_p\mu}) \geq 0, \tag{D. 11}$$

is satisfied, and this condition holds unless the heating rate is not too high to rise the temperature by factor 4/3 in the postshock flow.

The solution is is expressed as,

$$x = \frac{m_p\mu}{kT}v_2^2\left(2 + \sqrt{4 - \frac{kT}{m_p\mu v_2^2}}\right). \tag{D. 12}$$

After the gas cooled down to $kT/(m_p\mu) \ll v_2^2$, the collapse factor has the asymptotic value,

$$x = \frac{4v_2^2 m_p\mu}{kT}. \tag{D. 13}$$

Therefore the density is proportional to T^{-1} in this cooled region, and the pressure keeps constant. This limiting value of p is $4/3p_2$, which is not much diffrent form p_2. As a result, the postshock region is almost isobaric for wide a range of temperature.

References

[1] Bardeen,J.M., Bond,J.M., Kaiser,N. and Szalay, A.S., 1986, ApJ, **304**, 15,

[2] Bennett, D. P., et al., 1996, astro-ph/9606012 preprint

[3] Biniek, R.J. 1980, J.Phys.B, **13**, 4405,

[4] Blumenthal,G.R.,Faber,S.M.,Primack,J.R.,Rees,M.J.,1984, *Nature*,**311**, 517,

[5] Carlberg,R.G., 1981, MNRAS, **197**, 1021,

[6] Cen,R., Ostriker,J.P., 1993,ApJ, **417**, 404,

[7] Cen,R., Ostriker,J.P., 1993,ApJ, **417**, 415,

[8] Clayton, D. D. 1988, MNRAS, **234**, 1,

[9] Colella, P., Woodward, P. R. 1984, *Journal of Computational Physics*, **54**, 174,

[10] de Jong, T. 1972, A & A, **20**, 263,

[11] Driver, S. P. et.al. 1995, ApJ, 361, L1,

[12] Duley, W.W., Williams, D.A. 1984, *Interstellar Chemistry* (London:Academic Press)

[13] Efstathiou, G., Rees, M.J., 1988, MNRAS, **230**, 5,

[14] Eisenstein, D.J., Loeb, A., 1995, ApJ,**439**, 520,

[15] Glatzebrook, K. et.al. 1995, MNRAS, **273**, 157,

[16] Haehnelt, M.G., Rees, M.J., 1993, MNRAS, **265**, 727,

[17] Hayashi, C., Nakano, T. 1965, Prog. Theor. Phys., **34**, 754,

[18] Hollenbach,D., McKee,C., 1979, *Astrophys.J. Suppl.*, **41**, 55,

[19] Hunter, C., 1964, ApJ, **139**, 570,

[20] Hutchins,J.B., 1976 ApJ, **205**, 103,

[21] Inutsuka,S., Miyama,S.M., 1992, ApJ, **388**, 392,

[22] Izotov, Yu.I., Kolensnik, I.G.1984, Soviet Astro. **28**, No. 1, 15,

[23] Karpas,Z.,AAnicich, V., Huntress, W.T.,Jr. 1979, J.Chem.Phys., **70**, No.6, 2877,

[24] Katz, N., Gunn, J.E., 1991, ApJ, **377**, 365,

[25] Kauffmann, G., White, S.D.M. 1993, MNRAS, **261**, 921,

[26] Lahav, O., 1986, MNRAS, **220**, 259,

[27] Larson, R.B., 1985, MNRAS, **214**, 379,

[28] Lin, C.C., Mestel, L., Shu, F.H., 1965, ApJ, **142**, 1431,

[29] Lots, W. 1968, Zs.Phys., **216**,

[30] Low, C., Lynden-Bell, D. 1976, MNRAS, **176**, 367,

[31] Lynden-Bell, D. 1975, Vistas in Astronomy, **19**, 299,

[32] MacLow, M.-M., Shull, J. M. 1986, ApJ, **302**, 585,

[33] Matsuda, T., Sato, H., T.Takeda, H., 1965, *Prog.Theor.Phys.*, **42**, 219,

[34] Mitchell, G.F., Deveau, T.J. 1983, ApJ, **266**, 646,

[35] Miyama, S. M., Narita, S., Hayashi, C. 1987, Prog. Theor. Phys., **78**, 1051,

[36] Miyama, S. M., Narita, S., Hayashi, C. 1987, Prog. Theor. Phys., **78**, 1273,

[37] Nagasawa, M. 1987, Prog. Theor. Phys., **77**, 635,

[38] Nakamura, F. 1996, in preperation,

[39] Ostriker, J. 1964, ApJ, **140**, 1056,

[40] Palla,F.,Salpeter,E.E.,Stahler,S.W.,1983,ApJ, **271**,632.

[41] Peebles,P.J.E.,1993,*Principles of Phisical Cosmology*, (Princeton).

[42] Poularert, G., Brouillard, F., Claeys, W., McGowan, J.W., Van Wassenhove,G. 1978, J.phys., B, **11**, L671,

[43] Prasad,S.S., Huntress, W.T.,Jr. 1980, ApJSuppl., **43**,1,

[44] Puy, D., Signore, M. 1996, A & A, **305**, 371,

[45] Ramaker, D.E., Peek,J.,M. 1976, Phys.Rev. A, **13, 58,**

[46] Rees, M. J. 1976, MNRAS, **176**, 483,

[47] Rees,M.J., Ostriker,J.P., 1977, MNRAS, **179**, 541.

[48] Rocha-Pinto, H. J., Maciel, W. J. 1996, MNRAS, **279**, 447,

[49] Rybicki, G. B., & Lightman, A. P. 1979,
Radiative Process in Astrophysics (New York:Wiley-Interscience),

[50] Shapiro, P.R., Kang, H., 1987, ApJ, **318**, 32,

[51] Silk, J. 1977, ApJ, **211**, 638,

[52] Silk, J. 1977, ApJ, **214**, 152,

[53] Simon, R. 1965, Ann. d'Astrophys., **28**, 40,

[54] Sobelman,I,I., Vaninshtein, L.A., Yukov, E.V. 1981,*Excitation of Atoms and Broadning of Spectral Lines* (New York: Springer-Verlag),

[55] Sobelman,I,I. 1991 *Atomic Spectra and Radiative Transitions* (New York: Springer-Verlag),

[56] Spitzer, L. Jr., 1956, *The Physics of Fully ionized Gases(New York:Interscience)*, p.88

[57] Susa, H., Uehara, H., Nishi, R. 1996, Prog. Theor. Phys., to appear in vol.**96**,

[58] Susa, H., Sasaki, M., Tanaka, T., 1994, *Prog.Theor.Phys.*, **92**, 961,

[59] Turner, J., Kirby-Docken, K., Dalgarno, A., 1977, *Astrophys.J. Suppl.*, **35**, 281.

[60] Uehara, H.,Susa, H.,Nishi, R., T., Nakamura, M.,Yamada 1996,ApJ, **473**, L95,

[61] Umemura, M., 1993, ApJ, **406**, 361,

[62] White, S.D.M., 1984, ApJ, **286**, 38,

[63] Vader, J. P., de Jong, T. 1981, A & A, **100**, 124,

[64] Yoneyama, T. 1972, PASJ, **24**, 87,

[65] Yoshii, Y., Sabano, Y. 1979, PASJ, **31**, 305.